

Machine learning in drug development: Characterizing the effect of 30 drugs on the QT interval using Gaussian process regression, sensitivity analysis, and uncertainty quantification

Francisco Sahli Costabal^a, Kristen Matsuno^a, Jiang Yao^b, Paris Perdikaris^c, Ellen Kuhl^{a,*}

^a Department of Mechanical Engineering, Stanford University, Stanford, CA 94305, USA

^b Dassault Systèmes Simulia Corporation, Johnston, RI 02919, USA

^c Mechanical Engineering and Applied Mechanics, University of Pennsylvania, Philadelphia, PA 19104, USA

Received 13 July 2018; received in revised form 21 January 2019; accepted 23 January 2019

Available online 2 February 2019

Highlights

- Arrhythmias are a serious side effect of many drugs, not just of drugs for the heart.
- We show how 30 drugs affect the QT interval, a clinical indicator for cardiac arrhythmias.
- We create a surrogate model for the QT interval using Gaussian process regression.
- Using sensitivity analyses, we identify the relevant ion channels for QT interval prolongation.
- Using uncertainty quantification, we show how measurement variabilities affect our results.

Abstract

Prolonged QT intervals are a major risk factor for ventricular arrhythmias and a leading cause of sudden cardiac death. Various drugs are known to trigger QT interval prolongation and increase the proarrhythmic potential. Yet, how precisely the action of drugs on the cellular level translates into QT interval prolongation on the whole organ level remains insufficiently understood. Here we use machine learning techniques to systematically characterize the effect of 30 common drugs on the QT interval. We combine information from high fidelity three-dimensional human heart simulations with low fidelity one-dimensional cable simulations to build a surrogate model for the QT interval using multi-fidelity Gaussian process regression. Once trained and cross-validated, we apply our surrogate model to perform sensitivity analysis and uncertainty quantification. Our sensitivity analysis suggests that compounds that block the rapid delayed rectifier potassium current I_{Kr} have the greatest prolonging effect of the QT interval, and that blocking the L-type calcium current I_{CaL} and late sodium current I_{NaL} shortens the QT interval. Our uncertainty quantification allows us to propagate the experimental variability from individual block-concentration measurements into the QT interval and reveals that QT interval uncertainty is mainly driven by the variability in I_{Kr} block. In a final validation study, we demonstrate an excellent agreement between our predicted QT interval changes and the changes observed in a randomized clinical trial for the

* Corresponding author.

E-mail address: ekuhl@stanford.edu (E. Kuhl).

drugs dofetilide, quinidine, ranolazine, and verapamil. We anticipate that both the machine learning methods and the results of this study will have great potential in the efficient development of safer drugs.

© 2019 The Authors. Published by Elsevier B.V. This is an open access article under the CC BY license (<http://creativecommons.org/licenses/by/4.0/>).

Keywords: Machine learning; Gaussian process regression; Sensitivity analysis; Uncertainty quantification; Finite element analysis; Drug development

1. Introduction

Sudden cardiac death is an abrupt, unexpected loss of heart function. The majority of sudden cardiac deaths can be attributed to ventricular arrhythmias associated with a significant increase in heart rate and a loss of cardiac output [1]. A prolonged QT interval is a major risk factor for ventricular arrhythmias and sudden cardiac death [2]. The QT interval is a specific feature of the electrocardiogram that measures the total time from the beginning of the QRS complex to the end of the T wave associated with the depolarization and repolarization of the ventricles [3]. Many drugs, not just cardiac drugs, prolong the QT interval and induce a condition known as torsades de pointes, a ventricular arrhythmia characterized by rapid, irregular QRS complexes that oscillate around the electrocardiogram baseline [4]. Most episodes of torsades de pointes begin spontaneously and revert to normal sinus rhythm within a few seconds, but some persist, degenerate into ventricular fibrillation, and lead to sudden cardiac death [3]. In the United States, more than 350,000 sudden cardiac deaths occur each year, but the true incidence of drug-induced torsades de pointes is largely unknown [5]. In the early 1990s, the reporting rate of torsades de pointes increased exponentially when numerous drugs were recognized to have an increased pro-torsadogenic risk [6]. In response, 14 compounds were removed from the market. Currently, the gold standard to assess the pro-arrhythmic risk of a drug is to measure its effects on a specific potassium channel in single cell experiments [7] and on the QT interval in the electrocardiogram [8]. Yet, the precise correlation between drug-induced ion channel block on the cellular level and the QT interval on the whole organ level remains poorly understood.

Mathematical modeling and computational simulations can help to mechanistically understand and quantify the effect of drugs on the QT interval. A recent initiative of regulatory agencies, clinical practitioners, researchers and industry partners recommends to use computational simulation to characterize the pro-arrhythmic risk of new and existing drugs [9,10]. There have been several recent efforts in view of this goal: In a single cell model, a study simulated the effect of 31 compounds on the single cell action potential and predicted the individual risk categories of these drugs [11]. However, these models fail to capture the electrotonic coupling between individual cells that has a significant influence on the development of arrhythmias [12–15]. In a one-dimensional model of cardiac electrophysiology, other studies simulated the effect of drugs on the QT interval [16,17]. We have recently developed a high-resolution multi-scale model of the human heart to study drug-induced arrhythmias [18]. With this model, we have explored the critical concentrations at which drugs initiate torsades de pointes [19] and the mechanisms that trigger arrhythmias across the scales [15]. Yet, these high fidelity models still remain the exception and a major roadblock to use them more frequently is their tremendous computational cost.

The success of a computational drug safety evaluation heavily relies on experimental data that characterize the block-concentration response of specific drugs on specific ion channels [11]. Block-concentration characteristics are typically recorded in single cell patch clamp electrophysiology [20]. These experiments are inherently associated with uncertainties that propagate into the mathematical and computational models. This implies that the experimental measurements create an uncertainty in the output [21], in our case in the QT interval, that needs to be quantified. Various strategies have been proposed to address uncertainty including global optimization [22], data assimilation and genetic algorithms [23], causality and information flow [24], and phase transitions [25]. Specifically, recent studies have made first attempts to quantify the uncertainties of block-concentration measurements [26]. However, current efforts have focused exclusively on characterizing uncertainties on single cell level [27]. Because of the immense computational cost of uncertainty propagation, there is currently no strategy to propagate the uncertainties of block-concentration measurements from the cellular level into the QT interval on the whole heart level.

Here we use machine learning techniques to combine data from different levels of fidelity [28] and characterize the effect of drugs on the QT interval. We prototype a method that allows us to explore the QT interval at the organ level via sensitivity analysis and uncertainty quantification while keeping the computational cost manageable. **Fig. 1**

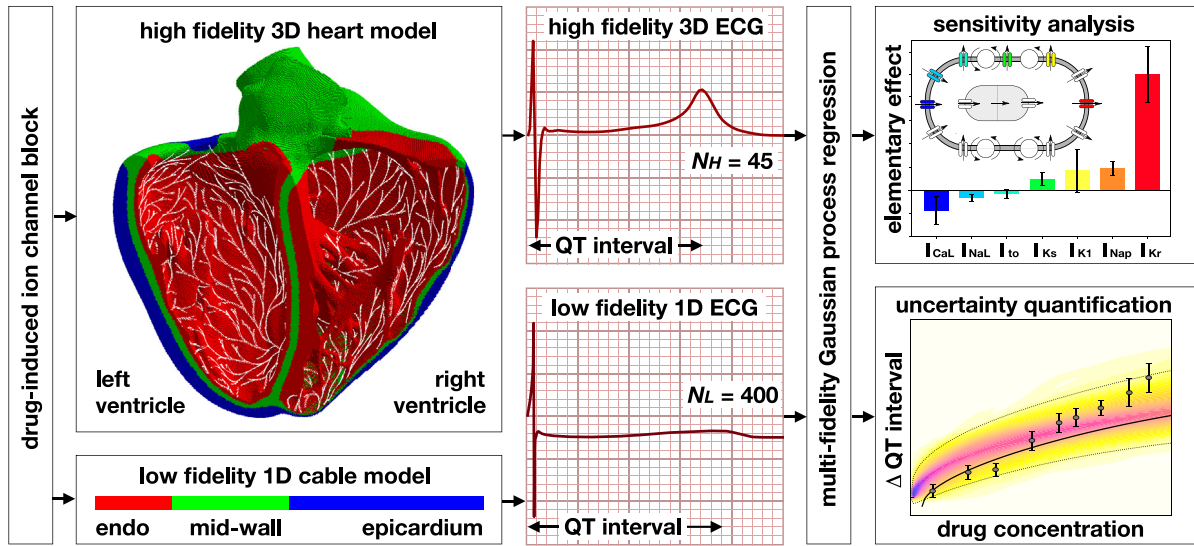


Fig. 1. Methods overview. Using machine learning techniques, we combine data from different levels of fidelity and characterize the effect of drugs on the QT interval. The input to our model are drug-induced channel block recordings from single cell patch clamp electrophysiology [20]. From this input, we simulate the effect of drugs using a high fidelity three-dimensional heart model [19] and a low fidelity one-dimensional cable model [15]. From $N_H = 45$ high and $N_L = 400$ low fidelity simulations, we calculate high and low fidelity electrocardiograms from which we extract the drug-modulated QT interval lengths. From these results, we build a surrogate model using multi-fidelity Gaussian process regression [29]. Once we have trained our regression, we perform a sensitivity analysis and propagate the uncertainty from the drug-induced channel block recordings into the QT interval.

illustrates the work flow of our method: Our input are drug-induced channel block recordings from single cell patch clamp electrophysiology [20]. From this input, we simulate the effect of drugs using finite element models of cardiac electrophysiology. We perform $N_H = 45$ high fidelity three-dimensional human heart simulations [19] and $N_L = 400$ low fidelity one-dimensional cable simulations [15], which we post-process to extract the electrocardiograms to quantify the drug-modulated QT interval lengths. We integrate these results into a surrogate model using multi-fidelity Gaussian process regression [29]. Once we have trained our regression, we perform a sensitivity analysis to identify the effect of individual channel blocks on the QT interval and propagate the uncertainty from the drug-induced channel block recordings into the QT interval. We anticipate that the results from this study will help understand the mechanisms behind drug-induced arrhythmias and improve the design of new compounds.

2. Methods

2.1. Cardiac electrophysiology

We model the spatio-temporal evolution of the transmembrane potential ϕ using the classical mono-domain model [30,31],

$$\dot{\phi} = \text{div}(\mathbf{D} \cdot \nabla \phi) + f^\phi \text{ on } \mathcal{B}. \quad (1)$$

We initialize the transmembrane potential with the initial conditions, $\phi(t = 0) = \phi_0$, and adopt homogeneous Neumann boundary conditions across the entire boundary, $(\mathbf{D} \cdot \nabla \phi) \cdot \mathbf{n} = 0$ on $d\mathcal{B}$. For the flux term, $\text{div}(\mathbf{D} \cdot \nabla \phi)$, we assume an anisotropic conductivity \mathbf{D} with a fast signal propagation of D^\parallel parallel to the fiber direction \mathbf{f} and a slow signal propagation of D^\perp perpendicular to it [32,33],

$$\mathbf{D} = D^\parallel \mathbf{f} \otimes \mathbf{f} + D^\perp [\mathbf{I} - \mathbf{f} \otimes \mathbf{f}]. \quad (2)$$

For the source term, f^ϕ , we scale the ionic current I_{ion} by the membrane capacitance C_m ,

$$f^\phi = -I_{\text{ion}}/C_m, \quad (3)$$

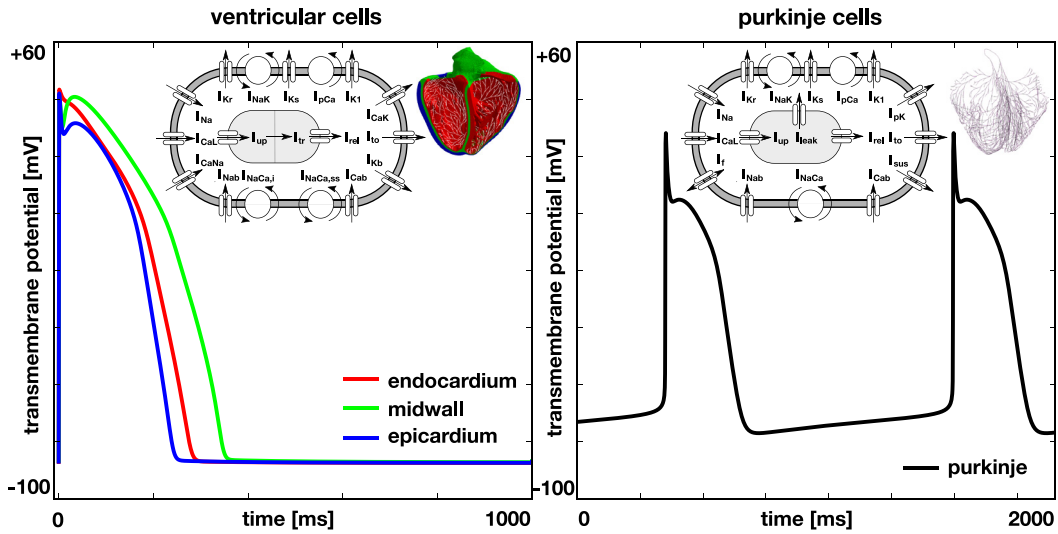


Fig. 2. Drug-induced ion channel block. Human ventricular cardiomyocytes model, left, and Purkinje fiber model, right. The ventricular cell model distinguishes between endocardial, midwall, and epicardial cells and has 15 ionic currents and 39 state variables [39]; the Purkinje cell model has 14 ionic currents and 20 state variables [42]. We selectively block ionic currents and determine the fractional block from single cell experiments [20] using a Hill model.

and model the ionic current $I_{ion}(\phi, \mathbf{q})$ as a function of the transmembrane potential ϕ and a set of state variables \mathbf{q} [34,35]. The state variables obey ordinary differential equations, $\dot{\mathbf{q}} = \mathbf{g}(\phi, \mathbf{q})$, as functions of the transmembrane potential ϕ and their current values \mathbf{q} [36]. The number of ionic currents and state variables depends on the cell type and determines the complexity of the model. Here we use two distinct cell types, ventricular cells and Purkinje cells.

2.2. Drug-induced ion channel block

We model the effect of drugs on the single cell action potential ϕ by selectively blocking the relevant ionic currents I_{ion} [37]. For each drug, we select a desired concentration C , calculate the fractional current block of individual channels β_i using a Hill model, and scale the ionic current I_i by the fractional block $[1 - \beta_i]$ [18],

$$I_i^{\text{drug}} = [1 - \beta_i] I_i \quad \text{with} \quad \beta_i = \left[1 + \left(\frac{C}{IC_{50}} \right)^h \right]^{-1}. \quad (4)$$

The Hill model has two parameters, the Hill exponent h and the concentration IC_{50} required to achieve a 50% current block. We identify these two Hill-type parameters h and IC_{50} for different drugs using fractional block measurements β_i at different discrete concentration levels C from patch clamp electrophysiology [20,26]. For the ventricular cells, we choose conductivities of $D^{\parallel} = 0.090 \text{ mm}^2/\text{ms}$ and $D^{\perp} = 0.012 \text{ mm}^2/\text{ms}$ parallel and perpendicular to the fiber direction [38] and adopt the O'Hara–Rudy model with 15 ionic currents and 39 state variables [39],

$$I_{ion} = I_{Kr} + I_{Ks} + I_{K1} + I_{CaL} + I_{Na} + I_{CaNa} + I_{CaK} + I_{Cab} + I_{Nab} + I_{Kb} + I_{to} + I_{NaK} + I_{pCa} + I_{NaCa,i} + I_{NaCa,ss}. \quad (5)$$

Fig. 2, left, shows the rapid and slow delayed rectifier potassium currents I_{Kr} and I_{Ks} , the inward rectifier potassium current I_{K1} , the L-type calcium current I_{CaL} , the fast and late sodium currents I_{NaP} and I_{NaL} , the calcium sodium and calcium potassium currents I_{CaNa} and I_{CaK} , the background calcium, sodium, and potassium currents I_{Cab} , I_{Nab} , and I_{Kb} , the transient outward potassium current I_{to} , the sodium potassium pump current I_{NaK} , the sarcolemmal calcium pump current I_{pCa} , and the sodium calcium exchange currents $I_{NaCa,i}$ and $I_{NaCa,ss}$ of the ventricular cell model. To appropriately model signal propagation [40], we replaced the fast sodium current I_{NaP} of the original model with the fast sodium current of the ten Tusscher model [41], without any changes in the model parameters.

To account for regional specificity, we use three individual parameterizations of the O'Hara–Rudy model for endocardial, midwall, and epicardial cells. For the Purkinje fiber network, we choose a conductivity of $D^{\parallel} = 3.0 \text{ mm}^2/\text{ms}$ [18] and adopt the Stewart model with 14 ionic currents and 20 state variables [42],

$$I_{\text{ion}} = I_{\text{Kr}} + I_{\text{Ks}} + I_{\text{K1}} + I_{\text{CaL}} + I_{\text{Na}} + I_{\text{Cab}} + I_{\text{Nab}} + I_{\text{to}} + I_{\text{f}} + I_{\text{sus}} + I_{\text{NaK}} + I_{\text{pCa}} + I_{\text{pK}} + I_{\text{NaCa}}. \quad (6)$$

Fig. 2, right, shows the rapid and slow delayed rectifier potassium currents I_{Kr} and I_{Ks} , the inward rectifier potassium current I_{K1} , the L-type calcium current I_{CaL} , the fast and late sodium currents I_{Na} , the background calcium and sodium currents I_{Cab} and I_{Nab} , the transient outward potassium current I_{to} , the hyperpolarization-activated current I_{f} , the sustained potassium current I_{sus} , the sodium potassium pump current I_{NaK} , the calcium and potassium pump currents I_{pCa} and I_{pK} , and the sodium calcium exchange current I_{NaCa} of the Purkinje fiber model.

2.3. High fidelity three-dimensional heart model

For the high fidelity model, we discretize the weak form of the mono-domain equation (1) in space using finite elements [30] and in time using finite differences [19]. To solve the resulting system of equations, we adopt the finite element software package Abaqus [43]. In particular, we use an explicit time integrator for both the reaction–diffusion equation (1) and the ionic models in Eqs. (5) and (6), with a fixed time step size of $\Delta t = 0.005 \text{ ms}$. Our high fidelity model is a fully three-dimensional representation of the human ventricles [44], created from magnetic resonance images [45], and discretized with regular cube elements with a constant edge length of 0.3 mm [19]. This results in a discretization with a total of 6,878,459 regular trilinear hexagonal finite elements, 7,519,918 nodes, and 268,259,901 internal variables. To model the regional specificity of ventricular cells, we create a transmural cell distribution with 20% endocardial cells, 30% midwall cells, and 50% epicardial discrete layers of cells [46] across the ventricular wall by simulating a series of Laplace problems [47]. We alternate essential boundary conditions in the endo- and epicardial surfaces and threshold the solution of these problems to create layers of tissue. This arrangement ensures positive T waves in the healthy baseline electrocardiogram [46]. We account for the anisotropy of the tissue by defining local orientations for each element [45]. To model the Purkinje fiber network, we generate a fractal tree that grows on the endocardial surface of the heart [48]. This results in a discretization with 39,772 linear cable elements, 39,842 nodes, and 795,440 internal variables [18]. At the terminals of the fractal tree, we connect the Purkinje network to the neighboring myocardium using 3545 resistor elements with a resistance of $1.78 \Omega\text{m}$ [38]. To explore how the single-cell action potentials from Fig. 2 translate into the excitation profile of the entire heart, we initially excite the Purkinje network at the location of the atrioventricular node and then let the automaticity of the Purkinje network drive the heart rate. We simulate five heart beats, which typically takes 40 h using 160 CPUs. We post-process the transmembrane potential profiles to calculate pseudo electrocardiograms [49]. At every point of the heart, we project the gradient of the transmembrane potential, $\nabla\phi$, onto the direction vector [50], $\nabla(1/\|\mathbf{r}\|)$, and integrate this projection across the entire cardiac domain \mathcal{B} [51], $\phi_e(\mathbf{x}_e) = -\int_{\mathcal{B}} \nabla\phi \cdot \nabla(1/\|\mathbf{r}\|) dV$. The vector $\mathbf{r} = \mathbf{x}_e - \mathbf{x}$ points from current point \mathbf{x} to a virtual precordial electrode \mathbf{x}_e two centimeters away from the left ventricular wall [19]. While the precise location of the electrode does modulate the amplitude of the electrocardiogram, it has virtually no impact on the length of the QT interval. From the final beat of the resulting electrocardiogram, we calculate the QT interval as the time difference between the onset of the QRS complex and the peak of the T wave [17]. Fig. 3 illustrates two characteristic simulations with our high fidelity model, one for the baseline case without drugs and one for the drug ranolazine.

2.4. Low fidelity one-dimensional cable model

For the low fidelity model, we discretize the set of continuum equations (1) to (5) in space and time using finite differences and adopt an explicit time integrator. Our low fidelity model is a one-dimensional cable representation of a transmural section across the ventricular wall [52]; it takes advantage of the existing parametrization of the O'Hara–Rudy model and ensures positive T waves [46]. The total length of the cable is 10 mm , in agreement with ventricular thicknesses from magnetic resonance studies [53]. We discretize the cable with a mesh size of 0.1 mm , resulting in a total of 101 nodes and 3900 internal variables [15]. Similar to the high fidelity model, we model the regional specificity of the ventricular wall using a distribution of 20% endocardial cells, 30% midwall cells, and 50% epicardial cells along the cable. To activate the cable, we excite the first endocardial cell at a frequency of 1 Hz , equivalent to 60 beats per

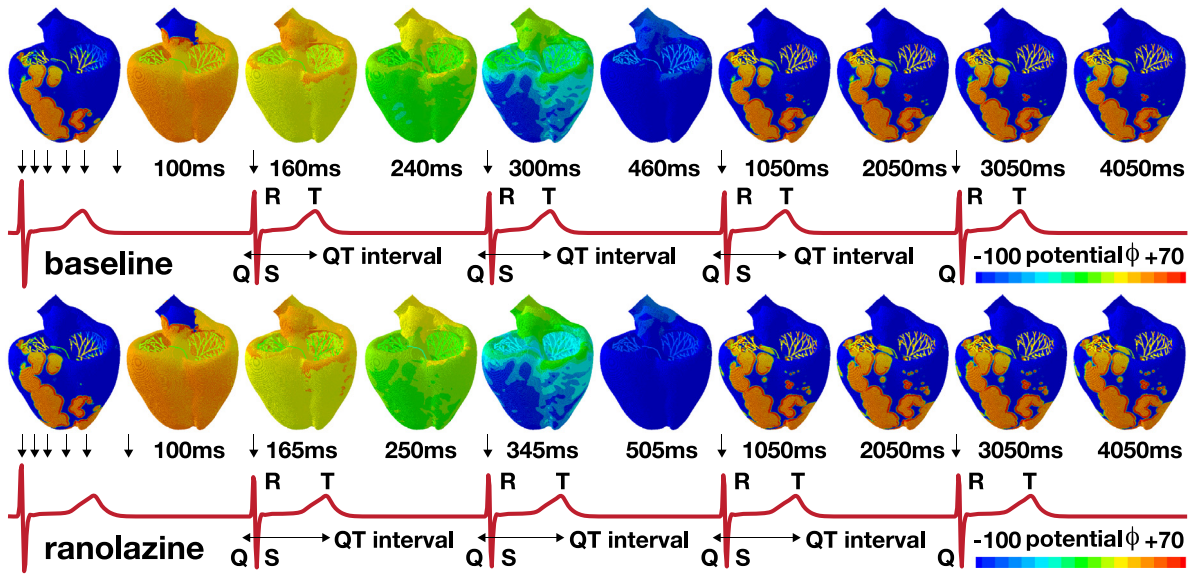


Fig. 3. High fidelity three-dimensional heart model. Our high fidelity model is a fully three-dimensional representation of the human ventricles discretized with 6,878,459 regular linear hexagonal finite elements, 7,519,918 nodes, and 268,259,901 internal variables [19]. For each high fidelity simulation, we simulate five heart beats, calculate the electrocardiogram, and extract the QT interval as the time difference between the onset of the QRS complex and the peak of the T wave [18].

minute, for a total of 100 beats using a fixed time step of 0.005 ms. After simulating 100 heart beats, we post-process the transmembrane potential profiles to calculate pseudo electrocardiograms by integrating the projected gradient of the transmembrane potential along the cable \mathcal{B} , $\phi_e(x_e) = -\int_{\mathcal{B}} \nabla \phi \cdot \nabla(1/r) dL$. Similar to the high fidelity model, $r = x_e - x$, denotes the distance from current point x to a virtual electrode x_e two centimeters away from the last epicardial cell. We define this quantity as the time difference between the initial excitation and the peak of the T wave [17].

2.5. Nonlinear Gaussian process regression

A core capability of the proposed methodology is associated with constructing probabilistic surrogate models that combine low- and high-fidelity information about the QT interval. This surrogate model will allow us to efficiently estimate QT intervals, perform sensitivity analyses, and propagate uncertainty in silico [54]. We construct our surrogate model using Gaussian process regression [55], a flexible tool for nonlinear Bayesian regression. We assume that we have a data-set of input/output pairs $\mathcal{D} = \{(x_i, y_i)_{i=1}^N\} = \{X, y\}$. The input $X \in \mathbb{R}^{N \times 7}$ contains the N measurements of the fractional current blocks β of the seven most relevant ionic currents, I_{CaL} , I_{Kr} , I_{Ks} , I_{K1} , I_{to} , I_{NaP} , and I_{NaL} [20,56], and the output $y \in \mathbb{R}^N$ contains the corresponding N QT intervals of the high fidelity, three-dimensional model. Our goal is to infer a latent function f , such that

$$y = f(X) + \epsilon, \quad (7)$$

where ϵ is a noise process that may corrupt our observations of y . For simplicity, we assume that ϵ is Gaussian and uncorrelated, $\epsilon \sim \mathcal{N}(\mathbf{0}, \sigma_n^2 \mathbf{I})$, where σ_n^2 is an unknown variance parameter that will be learned from the data, $\mathbf{0} \in \mathbb{R}^N$ is a zero column vector, and $\mathbf{I} \in \mathbb{R}^{N \times N}$ is the identity matrix. Starting from a zero-mean Gaussian process prior assumption on f ,

$$f(x) \sim \mathcal{GP}(\mathbf{0}, k(x, x'; \theta)), \quad (8)$$

we first identify the optimal set of kernel hyper-parameters and model parameters, $\Theta = \{\theta, \sigma_n^2\}$, and then use the optimized model to perform predictions at a set of new unobserved locations x^* . The covariance kernel function $k(x, x'; \theta)$ that depends on a set of hyper-parameters θ and encodes any prior belief or domain expertise we may

have about the underlying function f plays a central role in this process. Here we use the squared exponential covariance kernel with automatic relevance determination weights that account for anisotropy with respect to each input design variable [55]. We train our model by minimizing the negative log-marginal likelihood of the Gaussian process model [55]. Since our likelihood is Gaussian, we can evaluate it analytically in closed form,

$$\Theta^* = \arg \min_{\Theta} \mathcal{L}(\Theta) := \frac{1}{2} \log |\mathbf{K} + \sigma_n^2 \mathbf{I}| + \frac{1}{2} \mathbf{y}^T (\mathbf{K} + \sigma_n^2 \mathbf{I})^{-1} \mathbf{y} + \frac{N}{2} \log(2\pi), \quad (9)$$

where the covariance matrix $\mathbf{K} \in \mathbb{R}^{N \times N}$ follows from evaluating the kernel function $k(\cdot, \cdot; \theta)$ at the locations of the input training data \mathbf{X} . Here, we choose the squared exponential covariance kernel with automatic relevance determination weights for each input variable [55]. For the minimization, we adopt a quasi-Newton optimizer L-BFGS with random restarts [55,57]. We use the default parameters in the Scipy implementation [58]. Once we have trained our model on the available data, we compute the posterior predictive distribution $p(\mathbf{y}^* | \mathbf{x}^*, \mathcal{D}) \sim \mathcal{N}(\mu(\mathbf{x}^*), \Sigma(\mathbf{x}^*))$ at a new location \mathbf{x}^* by conditioning on the observed data,

$$\begin{aligned} \mu(\mathbf{x}^*) &= k(\mathbf{x}^*, \mathbf{X})(\mathbf{K} + \sigma_n^2 \mathbf{I})^{-1} \mathbf{y} \\ \Sigma(\mathbf{x}^*) &= k(\mathbf{x}^*, \mathbf{x}^*) - k(\mathbf{x}^*, \mathbf{X})(\mathbf{K} + \sigma_n^2 \mathbf{I})^{-1} k(\mathbf{X}, \mathbf{x}^*), \end{aligned} \quad (10)$$

where $\mu(\mathbf{x}^*)$ and $\Sigma(\mathbf{x}^*)$ denote the posterior mean and variance.

2.6. Multi-fidelity Gaussian processes regression

For multi-fidelity Gaussian processes regression, we extend the workflow of our nonlinear Gaussian process regression to data from different information sources of variable fidelity [59,60]. We introduce two levels of fidelity and observe data $\mathcal{D} = [\{(\mathbf{x}_L, y_L)_{i=1}^{N_L}\}, \{(\mathbf{x}_H, y_H)_{i=1}^{N_H}\}] = \{\mathbf{X}, \mathbf{y}\}$, where (\mathbf{x}_L, y_L) and (\mathbf{x}_H, y_H) are the input/output pairs generated by the low fidelity one-dimensional cable model and the high fidelity three-dimensional heart model, with significantly more data sets from the low than from the high fidelity model, $N_L \gg N_H$. We create a multi-variate regression framework that returns accurate high-fidelity predictions while being primarily trained on low-fidelity data and consider the following multi-output Gaussian process regression model [59],

$$\mathbf{y}_L = f_L(\mathbf{x}_L) + \epsilon_L \quad \text{and} \quad \mathbf{y}_H = f_H(\mathbf{x}_H) + \epsilon_H \quad (11)$$

where $\epsilon_L \sim \mathcal{N}(\mathbf{0}, \sigma_{n_L}^2 \mathbf{I})$ and $\epsilon_H \sim \mathcal{N}(\mathbf{0}, \sigma_{n_H}^2 \mathbf{I})$ denote the Gaussian and uncorrelated noise and $f_L(\mathbf{x})$ and $\delta(\mathbf{x})$ are two independent Gaussian processes,

$$\begin{aligned} f_L(\mathbf{x}) &\sim \mathcal{GP}(0, k_L(\mathbf{x}; \mathbf{x}'; \theta_L)) \\ \delta(\mathbf{x}) &\sim \mathcal{GP}(0, k_H(\mathbf{x}; \mathbf{x}'; \theta_H)) \quad \text{and} \quad f_H(\mathbf{x}) = \rho f_L(\mathbf{x}) + \delta(\mathbf{x}). \end{aligned} \quad (12)$$

The variances $\sigma_{n_L}^2$ and $\sigma_{n_H}^2$ that potentially corrupt the low- and high-fidelity data and the scaling parameter ρ are learned during model training. As a consequence of the auto-regressive assumption in Eq. (12), the joint distribution of the low- and high-fidelity data inherits the following structure,

$$\mathbf{y} = \begin{bmatrix} \mathbf{y}_L \\ \mathbf{y}_H \end{bmatrix} \sim \mathcal{N} \left(\begin{bmatrix} \mathbf{0} \\ \mathbf{0} \end{bmatrix}, \begin{bmatrix} K_{LL} & K_{LH} \\ K'_{LH} & K_{HH} \end{bmatrix} \right), \quad (13)$$

with

$$\begin{aligned} K_{LL} &= k_L(\mathbf{x}_L, \mathbf{x}'_L; \theta_L) + \sigma_{\epsilon_L}^2 \mathbf{I} \\ K_{LH} &= \rho k_L(\mathbf{x}_L, \mathbf{x}'_H; \theta_L) \\ K_{HH} &= \rho^2 k_L(\mathbf{x}_H, \mathbf{x}'_H; \theta_L) + k_H(\mathbf{x}_H, \mathbf{x}'_H; \theta_H) + \sigma_{\epsilon_H}^2 \mathbf{I}. \end{aligned} \quad (14)$$

The covariance of \mathbf{y} takes a block structure, where the diagonal blocks K_{LL} and K_{HH} model the data in each fidelity level and the off-diagonal blocks K_{LH} model the cross-correlation structure between different levels of fidelity. We can now train the model and perform posterior predictions using the concatenated low- and high-fidelity data along with this block covariance matrix structure that replaces \mathbf{K} in Eqs. (9) and (10). From minimizing the log-marginal likelihood in Eq. (9), we obtain the optimal set of model parameters and hyper-parameters, $\Theta = \{\theta_L, \theta_H, \rho, \sigma_{n_L}^2, \sigma_{n_H}^2\}$, with which we perform posterior predictions using Eqs. (10).

2.7. Training and cross-validation

To construct the Gaussian process regression, we limit the current blocks to the range $\beta_i \in [0.0, 0.6]$. Beyond this range, the high fidelity model may develop torsades de pointes [15,18,19], an arrhythmic condition in which the QT interval is no longer well defined. We compute the QT interval from $N_L = 400$ low fidelity one-dimensional cable simulations and from $N_H = 10$ high fidelity three-dimensional heart simulations using a latin hypercube design. We continue to sample the next $N_H = 35$ high fidelity points by adaptively choosing the location of maximum posterior variance, computed from the Gaussian process regression using Eq. (10). We do not account for the effect of rate changes in the QT interval, since we found, using the low fidelity model, that this change is on the order of 3%, and thus is rather small compared to the changes induced by drugs. To assess the accuracy of the constructed regression, we perform a five-fold cross-validation. We partition the $N_H = 45$ high fidelity samples into five groups and iteratively predict the response of one group on the basis of the remaining four. To quantify the predictive error of the regression, we calculate the root mean squared error for each group and average the result over all five groups, $\text{err} = \frac{1}{5} \sum_{i=1}^5 [\sum_{j=1}^N (f_i(X_j) - y_j)^2]^{1/2}$, where f_j is the Gaussian process regression that has been training with the remaining four groups and $N = N_H/5 = 9$.

2.8. Sensitivity analysis

To analyze the sensitivity of the QT interval with respect to different ion channel blocks, we adopt the elementary effects method [61,62]. We create a grid of p levels in the parameter space and sample by moving through trajectories that randomly change one parameter at a time to compute the elementary effect d_i associated with changes in the i th parameter,

$$d_i(X) = \frac{y(X_1, \dots, X_{i-1}, X_i + \Delta, X_{i+1}, \dots, X_D) - y(X)}{\Delta}. \quad (15)$$

Here $y = f(X)$ is the output of the multi-fidelity Gaussian process regression, rather than the output of the model itself, and $\Delta = g/(1 - p)$ in terms of the number of levels to jump in the next move in the trajectory g , typically $g = p/2$. We calculate the mean μ_i and standard deviation σ_i of the elementary effect $d_i(X_r)$ for each of the seven channel blocks β_i [61],

$$\mu_i = \frac{1}{N_t} \sum_{r=1}^{N_t} d_i(X_r) \quad \text{and} \quad \sigma_i = \left[\frac{1}{N_t - 1} \sum_{r=1}^{N_t} (d_i(X_r) - \mu_i)^2 \right]^{1/2}. \quad (16)$$

The mean μ_i represents the average influence of the input, the channel block β_i , on the output, the QT interval and the standard deviation σ_i indicates the degree of non-linearity and interaction of the QT interval when varying the channel block β_i . To overcome a well-known short-coming of the calculation of the mean μ_i , in which elementary effects with opposite signs cancel one another, we report the mean of the absolute value of the elementary effects [62],

$$\mu_i^* = \frac{1}{N_t} \sum_{r=1}^{N_t} |d_i(X_r)|. \quad (17)$$

We set the number of trajectories to 10,000 and the number of levels to six. Since the evaluation of the regression is rather inexpensive compared to the evaluation of the model itself, we can simply evaluate a large number of trajectories without having to choose optimal trajectories, which would require the solution of a brute force problem [62].

A source of error is associated with the randomized selection of trajectories that may not cover the input parameter space evenly. We calculate the variance generated by this error using bootstrap [63] and sample with a replacement B times from the already calculated elementary effects, creating a distribution of μ_i , μ_i^* and σ_i . A second source of error is associated with using a surrogate model, the regression, instead of the model itself. To assess the magnitude of this error, we take advantage of the Gaussian process regressions that outputs a distribution rather than a single value. We compute the sensitivity indices N_z times and sample the values of the QT interval from a predictive posterior distribution [63]. This results in a matrix of $N_z \times B$ evaluations of the sensitivity indices, from which we compute the total variance σ_T^2 ,

$$\bar{\mu}_i^* = \frac{1}{(BN_z)} \sum_{b=1}^B \sum_{z=1}^{N_z} \mu_{ibz}^* \quad \text{and} \quad \sigma_T^2(\mu_i^*) = \frac{1}{BN_z - 1} \sum_{b=1}^B \sum_{z=1}^{N_z} (\mu_{ibz}^* - \bar{\mu}_i^*)^2. \quad (18)$$

We set the number of bootstrap repeats to $B = 100$ [63], the number of evaluations from the posterior distribution to $N_z = 500$, and the level of confidence to 95%. To quantify the influence of one of the model inputs over the output when all other input parameters are averaged [64], we compute the main effects of each channel block β_i using our surrogate model, $z(X_i) = E(y|X_i) - E(y)$. We approximate this metric using 200 samples from a latin hypercube design over the parameter space, $z(X_i) = 1/N \sum_{j=1}^N y(X_{1,j}, \dots, X_i, \dots, X_{D,j}) - 1/N \sum_{j=1}^N y(X_j)$, where X_j represents a sample from the latin hypercube. We vary the input X_i to compute the main effects across the parameter space.

2.9. Uncertainty quantification

To characterize the uncertainty in the Hill model parameters, the Hill exponent h and the concentration IC_{50} required to achieve a 50% current block in Eq. (4), we perform a systematic uncertainty quantification. We employ a hierarchical Bayesian approach to obtain a complete probabilistic characterization of the unknown Hill model parameters and obtain the posterior distribution of the parameters using Bayes' rule,

$$p(\theta|y) = \frac{p(y|\theta) p(\theta)}{\int p(y|\theta) p(\theta) d\theta}, \quad (19)$$

where $p(y|\theta)$ is the likelihood of the parameters θ for the observed data y , and $p(\theta)$ is the prior distribution of the parameters θ that contains our prior knowledge about the parameters before observing any data. We postulate the following prior distributions over the Hill exponent h , the inhibitory concentration IC_{50} , and the observed data y [26],

$$h_i \sim \log\text{-logistic}(\alpha, \beta) \quad IC_{50i} \sim \text{logistic}(\mu, s) \quad y_i^j \sim (f(x_i^j; h_i, IC_{50i}), \sigma^2) \quad (20)$$

where y_i^j is the j th concentration entry in experiment i 's responses y_i . We implicitly assume that every experiment i that generates a QT interval as an output y_i has K_i data points. This allows us to consider cases where different experiments may test different numbers of concentrations, $j = 1, \dots, K_i$ and $i = 1, \dots, N_e$. We employ experimental block-concentration data to obtain a posterior distribution over unknown parameters $\theta := \{\alpha, \beta, \mu, s, \sigma^2\}$ by assigning a gamma prior to each parameter $\{\alpha, \beta, \mu, s, \sigma^2\}$, and marginalizing it out using an adaptive Metropolis–Hastings MCMC algorithm [26]. This generates an approximate posterior distribution, $p(\theta|y)$, that we sample to consistently propagate the uncertainty associated with the Hill model parameters h and IC_{50} to the uncertainty associated with the predictions of the QT interval using our multi-fidelity framework. As basic input, we use previously published experimental data [20], in which ion channel currents were evaluated using whole-cell patch-clamping. Using the hierarchical Bayesian approach in conjunction with these data, we sample a set of 500 $\{h, IC_{50}\}$ parameter pairs. For each pair at each drug concentration, we calculate the fractional block β_i of a specific ion channel using Eq. (4) and feed it into the multi-fidelity regression of the QT interval. Finally, we obtain a probability density function using Gaussian kernel density estimation. We consider a range of normalized concentrations $C \in [0, \dots, 4 C_{\max}]$ and vary the concentration in increments of 0.1 C_{\max} , where C_{\max} is the free plasma concentration, the amount of the drug that is available to bind to the ion channel [20]. We determine the probability density as a function of both the compound concentration and the QT interval. For some compounds, the specified range of concentrations exceeds the range $\beta_i \in [0.0, 0.6]$ for which we had built our multi-fidelity regression. In these cases, we refrain from reporting the results due to the lack of validation. For all remaining QT intervals, we report the percentage QT interval change with respect to the baseline QT interval of 264 ms for the simulation without drugs.

3. Results

We successfully built a surrogate model using multi-fidelity Gaussian process regression and trained the model with high and low fidelity simulations. We used our surrogate model to perform sensitivity analysis and uncertainty quantification, and validated our results against experimental data.

3.1. Multi-fidelity Gaussian process regression and cross-validation

Our Gaussian process-based surrogate model combines high and low fidelity simulations to efficiently and accurately predict QT interval lengths. Fig. 4 shows the electrocardiograms generated by our high and low

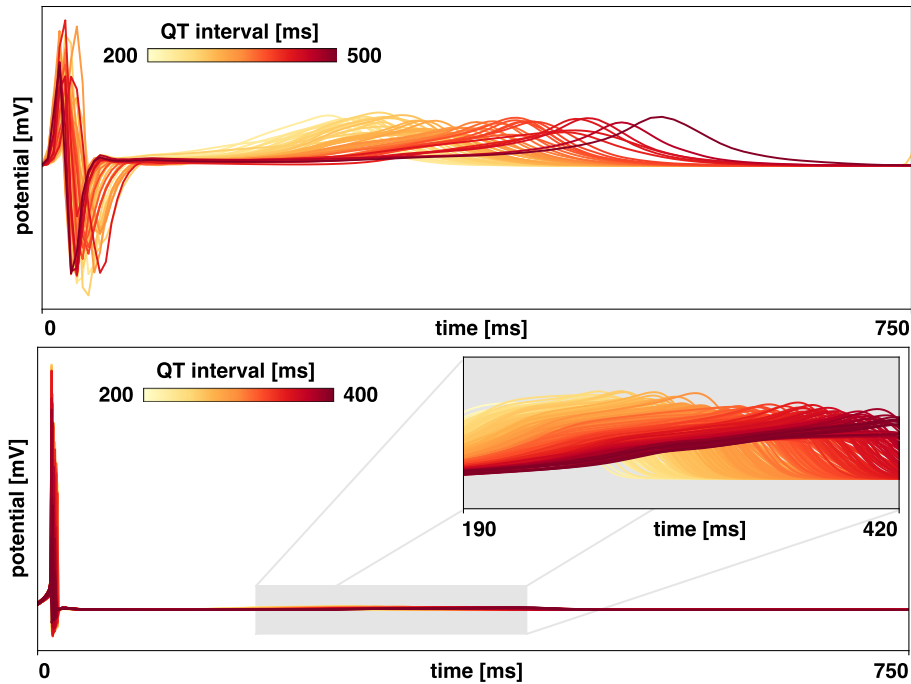


Fig. 4. Multi-fidelity Gaussian process regression. We combine the electrocardiograms of $N_H = 45$ high fidelity three-dimensional heart simulations, top, with $N_L = 400$ low fidelity one-dimensional cable simulations, bottom, to extract QT intervals for our multi-fidelity Gaussian process regression.

fidelity models. To calculate the QT intervals for our multi-fidelity Gaussian process regression, we combine $N_H = 45$ high fidelity three-dimensional heart simulations, top, with $N_L = 400$ low fidelity one-dimensional cable simulations, bottom. All electrocardiograms display the characteristic QRS complex followed by a positive T wave. The electrocardiograms of the low fidelity model show a narrow QRS complex and a small amplitude T wave compared to the electrocardiograms from the high fidelity model. The QT interval of the low fidelity model ranges from 196 to 411 ms and is smaller than the QT interval of the high fidelity model that ranges from 245 to 535 ms. This difference is a result of the irregular cell distribution of the high fidelity model. However, the different lengths have no influence on the training process, since the algorithm is set to find correlations between the different levels of fidelity as indicated in Eq. (12). A five-fold cross-validation of the multi-fidelity regression reveals an average root mean squared error of 16.7 ms, which represents a 6.3% error compared to the baseline QT interval of 264 ms.

3.2. Sensitivity analysis

Blocking I_{Kr} , I_{Nap} , I_{K1} and I_{Ks} prolongs the QT interval, while blocking I_{to} , I_{NaL} and I_{CaL} shortens the QT interval. Fig. 5 and Table 1 summarize the sensitivity of the QT interval with respect to individual current blocks from our elementary effects analysis. The analysis reveals that blocking the rapid delayed rectifier potassium current I_{Kr} , the fast sodium currents I_{Nap} , the inward rectifier potassium current I_{K1} , and the slow delayed rectifier potassium current I_{Ks} prolongs the QT interval, while blocking the transient outward potassium current I_{to} , the late sodium current I_{NaL} and the L-type calcium current I_{CaL} shortens the QT interval. Table 1 summarizes the means μ and variances σ of our elementary effect analysis in Fig. 5. Although the variances σ_M induced by our surrogate model account for a large part of the total variances σ_T , their overall values remain small compared to the magnitude of the elementary indices μ themselves. This suggests that our Gaussian process-based surrogate model provides a reasonably accurate approximation of the drug-induced changes in the QT interval.

The QT interval is most sensitive to drugs that block the rapid delayed rectifier potassium current I_{Kr} . Fig. 6 highlights the results of our main effects analysis for the QT interval of individual current blocks. To create these

Table 1

Sensitivity of QT interval with respect to individual current blocks. Blocking the I_{Kr} , I_{Nap} , I_{K1} and I_{Ks} currents prolongs the QT interval; blocking the I_{to} , I_{NaL} and I_{CaL} currents shortens the QT interval. Elementary effect indices are normalized with respect to the largest index I_{Kr} . Signs of the modified mean of the elementary effect index μ^* are assigned from μ . Variances σ induced by using the surrogate model are small compared to the indices μ^* themselves.

		I_{CaL}	I_{NaL}	I_{to}	I_{Ks}	I_{K1}	I_{Nap}	I_{Kr}
μ^*	[-]	-0.18	-0.07	-0.03	0.10	0.17	0.19	1.00
σ_N	[-]	0.0009	0.0003	0.0002	0.0006	0.0009	0.0007	0.0023
σ_M	[-]	0.0018	0.0003	0.0002	0.0003	0.0012	0.0035	0.0005
σ_T	[-]	0.0020	0.0004	0.0003	0.0006	0.0015	0.0035	0.0023

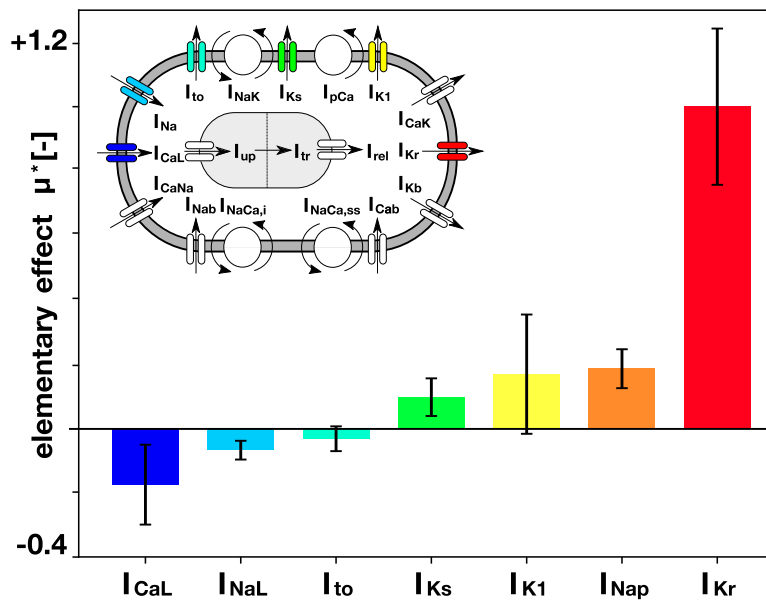


Fig. 5. Sensitivity of QT interval with respect to individual current blocks. Blocking the I_{Kr} , I_{Nap} , I_{K1} and I_{Ks} currents prolongs the QT interval; blocking the I_{to} , I_{NaL} and I_{CaL} currents shortens the QT interval. Blocking the rapid delayed rectifier potassium current I_{Kr} has the largest effect on the QT interval. Bars represent the modified mean of the elementary effect index μ^* , signs are assigned from μ , error bars represent the standard deviation σ .

results, we sampled the parameter space by moving through 200 trajectories that randomly change one parameter at a time to compute the main effect associated with changes in the respective parameter. The individual trajectories are displayed as gray lines and their average mean effect is shown in color. Our main effects analysis supports the results of the elementary effects analysis in Fig. 5 and Table 1. In addition, it provides information about the nonlinearity of the QT interval change with respect to the degree of blockage, which we show here for 0% to 60% block. Additionally, the spread of the gray lines indicates how much the interaction with other blockages affects an individual current block. Four channel blocks tend to prolong the QT interval, I_{Kr} , I_{Nap} , I_{K1} , and I_{Ks} : Blocking the rapid delayed rectifier potassium current I_{Kr} has the largest effect on the QT interval as already suggested by Fig. 5. Interestingly, this effect is highly nonlinear and increases as the degree of blockage increases as indicated by Fig. 6. Blocking the fast sodium current I_{Nap} also prolongs the QT interval, but the effect is less pronounced than I_{Kr} . The fast sodium current is responsible for the fast upstroke of the action potential and is active during the depolarization stage. Unlike the rapid delayed rectifier potassium current, it causes QT prolongation by widening the QRS complex, rather than by delaying the repolarization phase. Blocking the inward rectifier potassium current I_{K1} exhibits a pronounced non-linear behavior. Interestingly, at a low percentage block, I_{K1} blockage increases the QT interval, whereas at higher degrees of blockage, between 25% to 50%, the effect changes sign and blockage decreases the QT interval. Blocking the slow delayed rectifier potassium current I_{Ks} only has a minor effect on the QT interval with little interaction with

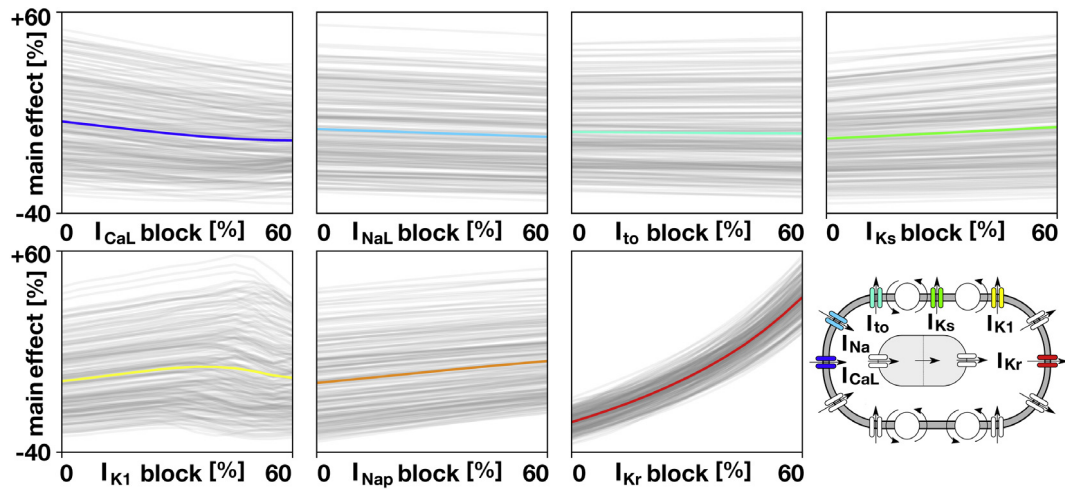


Fig. 6. Main effects analysis of QT interval for individual current blocks. Blocking the rapid delayed rectifier potassium current I_{Kr} prolongs the QT interval the most; blocking the L-type fast calcium current I_{CaL} decreases the QT interval the most. Gray lines represent the 200 trajectories used for the simulation, colored lines represent the average main effect. (For interpretation of the references to color in this figure legend, the reader is referred to the web version of this article.)

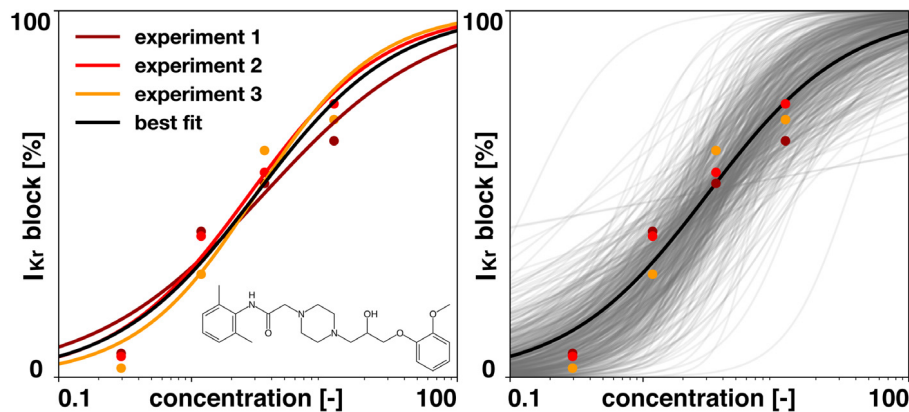


Fig. 7. Uncertainty quantification in block-concentration characteristics of the drug ranolazine. For three different experiments of ranolazine-induced blockage of the rapid delayed rectifier potassium current I_{Kr} [20], we calibrate three sets of Hill parameters (brown, red, and orange curves) and perform a best fit for all three experiments (black curve). To account for the uncertainty in the data, we use a hierarchical Bayesian model and infer a posterior distribution of the Hill model parameters to generate 500 Hill curves (gray curves). (For interpretation of the references to color in this figure legend, the reader is referred to the web version of this article.)

other current blocks, as we conclude from both the standard deviations σ in Fig. 5 and the almost flat lines in Fig. 6. Three channel blocks tend to shorten the QT interval, I_{to} , I_{NaL} , and I_{CaL} : Blocking the transient outward potassium current I_{to} and the late sodium current I_{NaL} moderately decrease the QT interval mostly linearly. Both display a small dependence on the level of block of other channels indicated by the parallel lines in Fig. 6. Blocking the L-type calcium current I_{CaL} has the strongest shortening effect on the QT interval. As Fig. 6 suggests, this effect is dependent on blockage of the other currents. Strikingly, some trajectories even display a positive slope indicating a QT interval prolongation when combined with other channel blocks.

3.3. Uncertainty quantification

Hierarchical Bayesian modeling provides estimates for the Hill model parameters of our block-concentration characteristics. Fig. 7 summarizes the result of three different experiments to characterize the ranolazine-induced

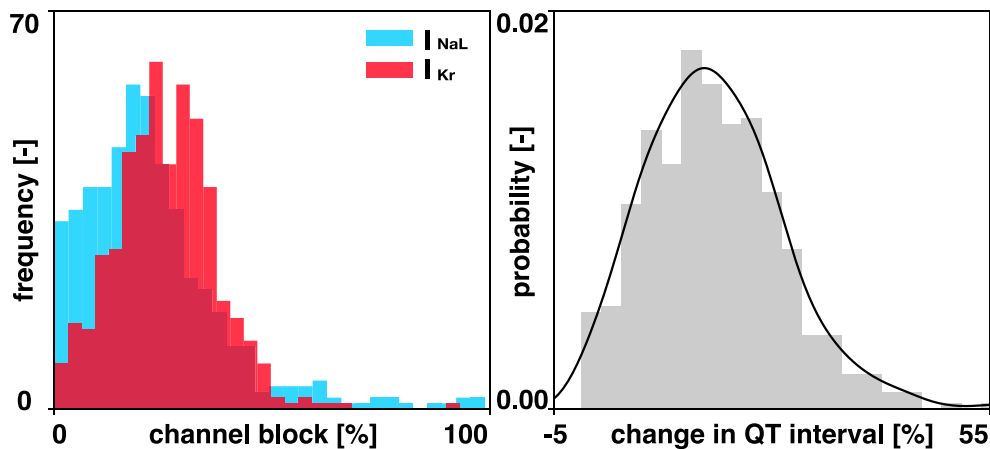


Fig. 8. Uncertainty propagation of block-concentration characteristics for ranolazine at its free plasma concentration into the QT interval. We apply the posterior distribution of current block from the hierarchical Bayesian model, left, to our surrogate model and propagate the uncertainty into the QT interval. From this QT interval distribution, we compute a probability density function, right, using a Gaussian kernel density estimation. For clear visualization, we only plot the channels with significant blockage, the rapid delayed rectifier potassium current I_{Kr} and the late sodium current I_{NaL} .

blockage of the rapid delayed rectifier potassium current I_{Kr} [20]. The points indicate the discrete measurements, the brown, red, and orange curves indicate the calibrated Hill models, and the black curve is the best fit Hill model for all three experiments combined. The experimental data display a significant inter-experiment variability and neither the individual fits nor the best fit Hill model can approximate the data reasonably well. We therefore used hierarchical Bayesian modeling to recapitulate the uncertainty in the data using prior information of the distribution of the Hill model parameters [26]. This resulted in a posterior distribution from which we sampled 500 pairs of Hill parameters $\{IC_{50}, h\}$ to construct 500 block-concentration curves for varying ranolazine concentrations. Fig. 8 illustrates how uncertainties of the block-concentration characteristics for ranolazine at its free plasma concentration propagate into the QT interval. To create these characteristics, we used the posterior distribution of the Hill parameters from the hierarchical Bayesian model in Fig. 7 and propagated the uncertainty using our Gaussian process-based surrogate model to calculate the distribution of the QT interval. The compound ranolazine primarily blocks the rapid delayed rectifier potassium current I_{Kr} and the late sodium current I_{NaL} . Fig. 8, left, confirms that our predictions with the hierarchical Bayesian model accurately capture these effects. We then propagated this uncertainty into the QT interval. This resulted in a QT interval distribution that highlights a spread of possible values. Fig. 8, right, shows this distribution, and, in addition, the probability density function for the QT interval that we computed using a Gaussian kernel density estimation.

Uncertainties in the experimentally measured block-concentration characteristics for 30 compounds propagate into the QT interval. Fig. 9 shows how the uncertainties of the block-concentration characteristics for 30 compounds at their free plasma concentration propagate into the QT interval. Uncertainties in the individual block-concentration characteristics in columns one through seven translate into uncertainties in the QT interval in column eight. In agreement with our sensitivity analysis in Fig. 5, uncertainties in the rapid delayed rectifier potassium current I_{Kr} in column seven have the greatest influence on the uncertainty of the QT interval. For example, compound nilotinib in row four displays a 95% confidence interval for a rapid delayed rectifier potassium current I_{Kr} block of 0.0 to 81.4%, which translates into a 95% confidence interval for the QT interval change of -5.8% to 72.8% . In contrast, the compound diltiazem in row thirty exhibits high variability in the L-type calcium current I_{CaL} block with a 95% confidence interval of 15.2% to 88.6%, which translates into a smaller uncertainty in the QT interval change of with a 95% confidence interval -11.3% to 0.2% .

At the free plasma concentration, dofetilide, flecainide, and quinidine change in the QT interval by more than 50%. Fig. 10 summarizes the probability density of a QT interval change for 30 compounds across a range of normalized compound concentrations. For some compounds including amiodorane, amitriptyline and toremifene, increasing the concentration has only minor effects on the QT interval; for others, including diltiazem and rufinamide,

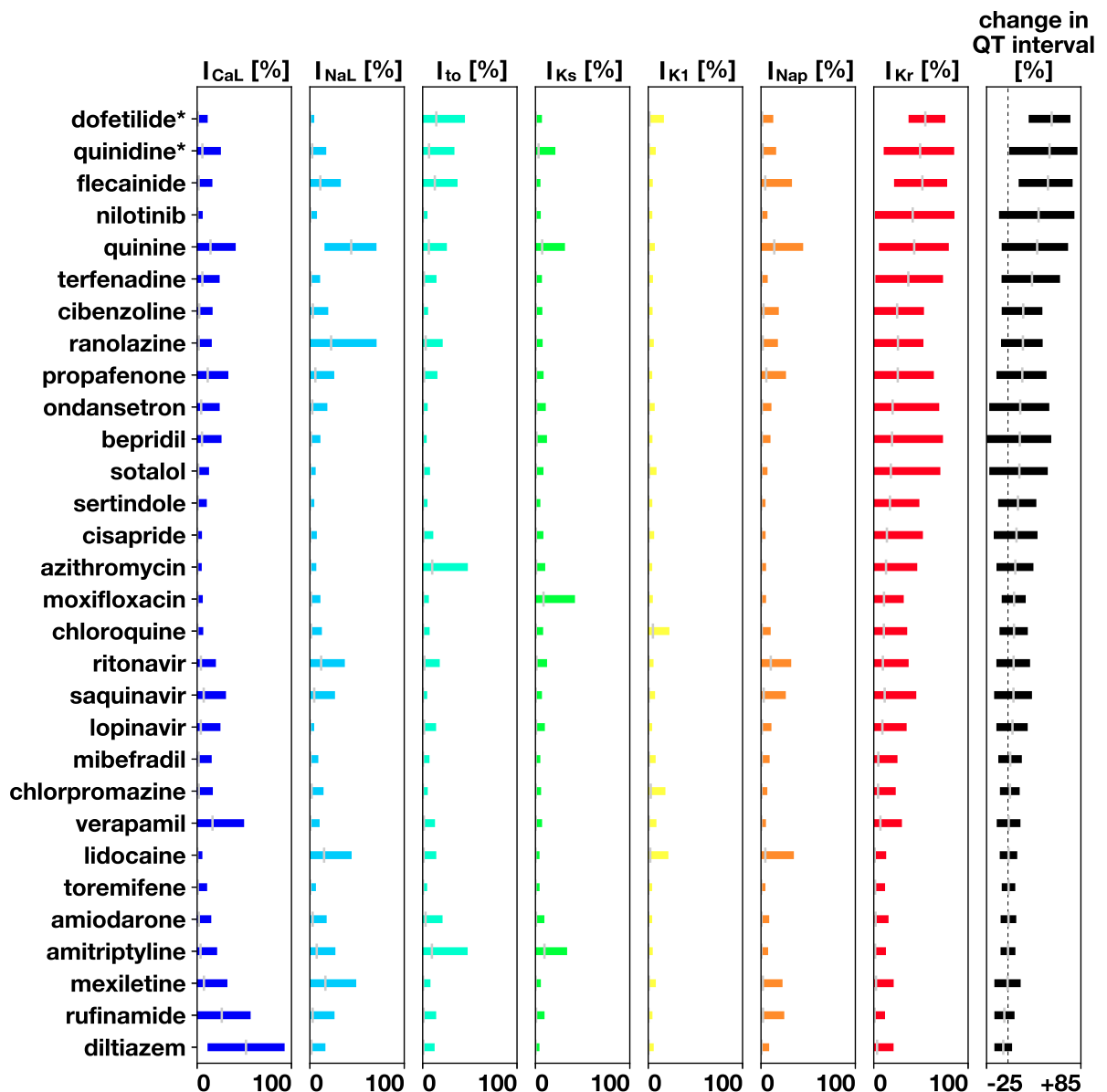


Fig. 9. Uncertainty propagation of block-concentration characteristics for 30 compounds at their free plasma concentration into the QT interval. Color bars indicate the 95% confidence intervals and gray lines indicate the mean. All drugs are displayed at their free plasma concentration C_{max} , except dofetilide* and quinidine*, which are displayed at $0.9 C_{max}$ and $0.4 C_{max}$ to avoid extrapolation. (For interpretation of the references to color in this figure legend, the reader is referred to the web version of this article.)

the QT interval tends to decrease with increasing concentration. However, for most compounds, increasing the concentration increases the QT interval. The QT interval is particularly responsive to increases in the concentration of dofetilide, flecainide, and quinidine. These compounds raise the average change in the QT interval by 50% or more by the time they reach their free plasma concentration. Gray regions indicate that the blocks are beyond the values used to train the Gaussian process regression. For all compounds, the uncertainty in the predictions of the QT interval tends to increase with increasing concentration. In general, the regions of highest probability are located near zero concentrations, since the Hill model is designed to predict zero block for zero concentration. Notably, the uncertainty tends to stabilize at higher concentrations for most cases, with the exception of mexiletine.

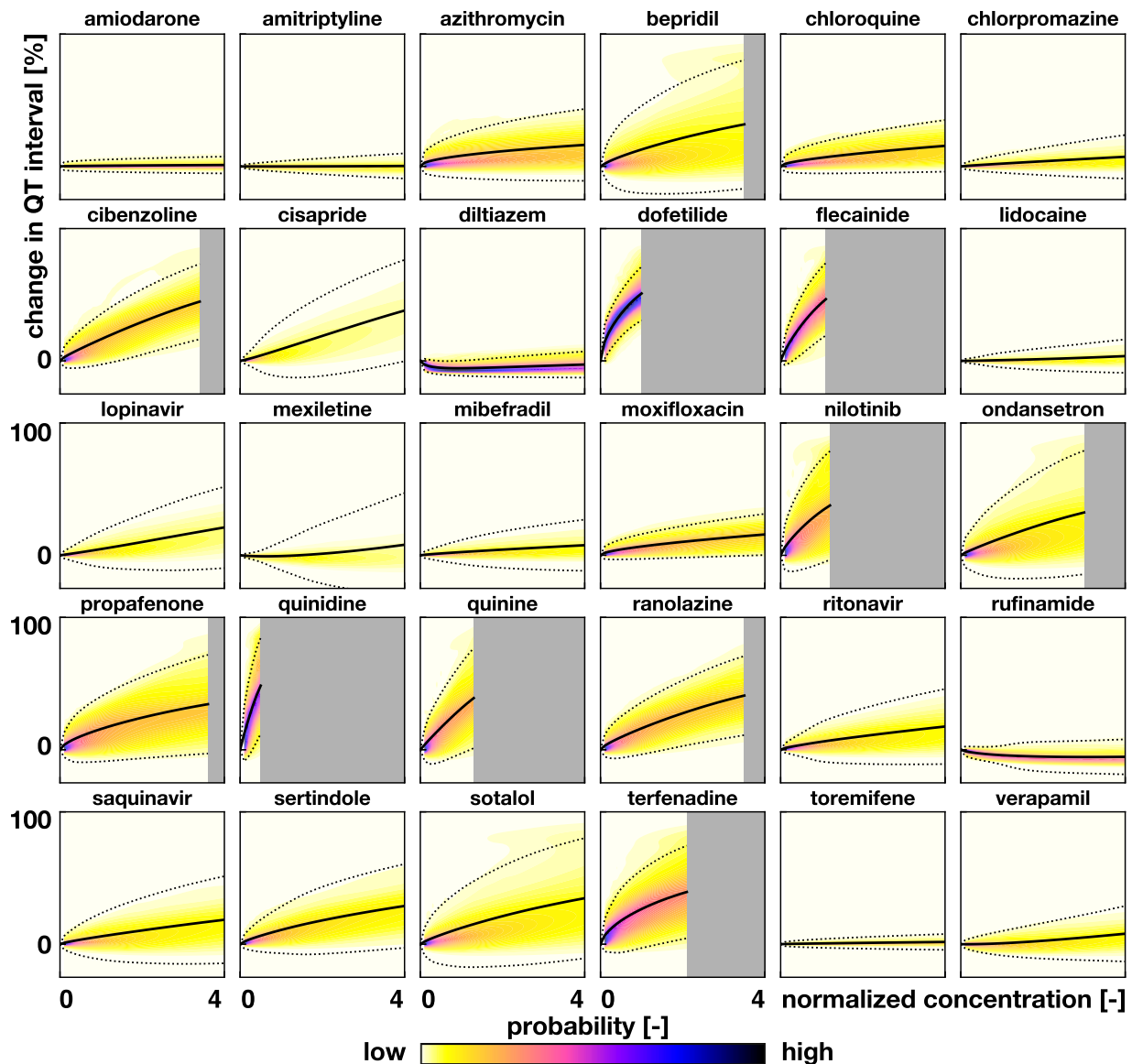


Fig. 10. Probability of QT interval change for 30 compounds across a range of compound concentrations. Mean QT interval changes are shown as solid black lines and 95% confidence intervals are shown as dotted lines; gray regions are used when the blocks exceeded the range used to build the surrogate model.

3.4. Validation

Our model predictions show excellent agreement with a randomized clinical trial for dofetilide, quinidine, ranolazine, and verapamil. To validate the predictions of our surrogate model, we use data from a randomized clinical trial that reports QTc interval changes for different concentrations of four common compounds: dofetilide, quinidine, ranolazine and verapamil [65]. These compounds present an ideal set for our model validation, since they selectively block the most relevant channels according to our sensitivity analysis: dofetilide blocks the rapid delayed rectifier potassium current I_{Kr} ; quinidine primarily blocks the rapid and slow delayed rectifier potassium currents I_{Kr} and I_{Ks} and the transient outward potassium current I_{to} ; ranolazine blocks the rapid delayed rectifier potassium current I_{Kr} and the late sodium current I_{NaL} ; and verapamil blocks the rapid delayed rectifier potassium current

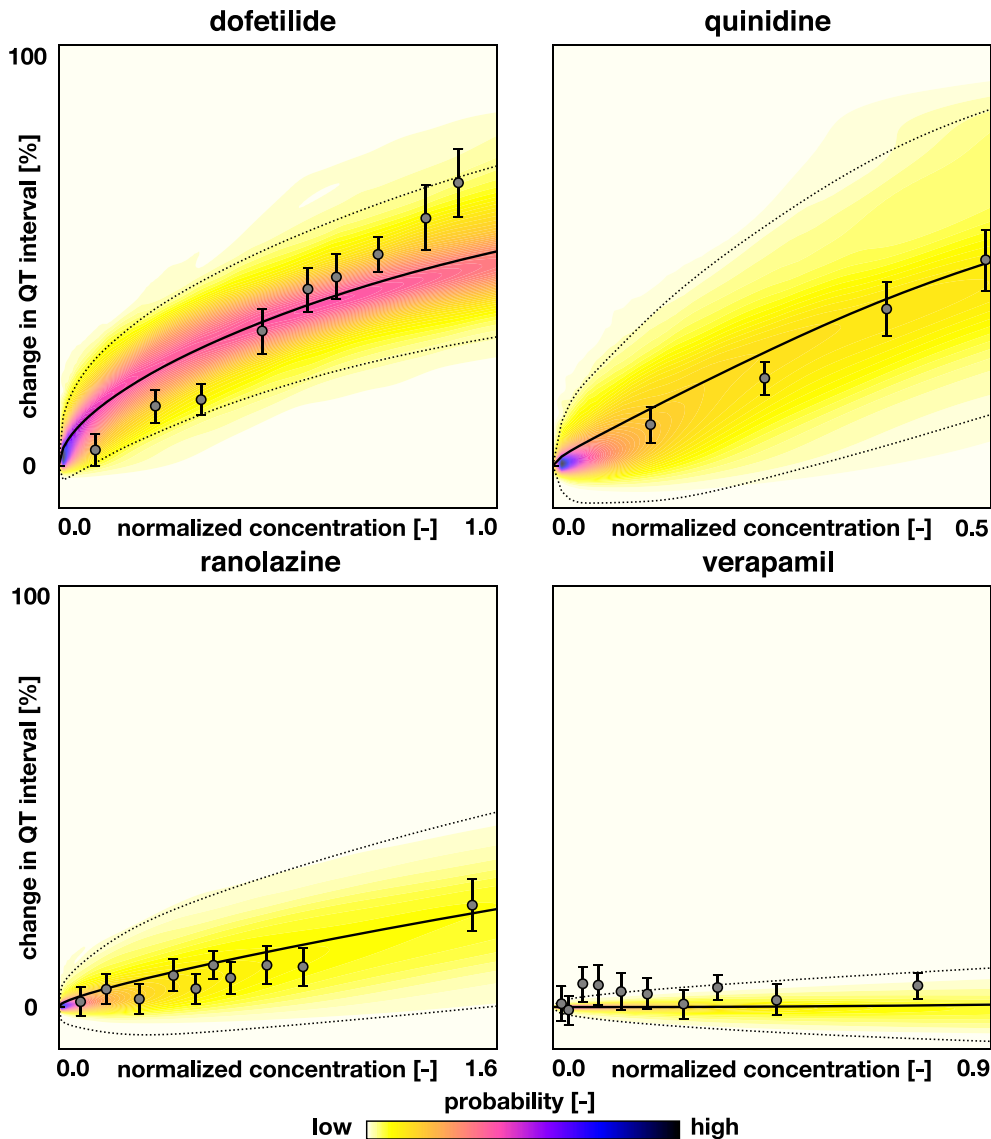


Fig. 11. Validation of QT interval change predictions for the compounds dofetilide, quinidine, ranolazine, and verapamil. These compounds block channels with opposing effects on the QT interval. Dofetilide is a selective I_{K_r} blocker, quinidine primarily blocks I_{K_r} , I_{to} and I_{K_s} , ranolazine blocks I_{NaL} and I_{K_r} , and verapamil blocks I_{CaL} and I_{K_r} . Mean QT interval changes are shown as solid black lines and 95% confidence intervals are shown as dotted lines; gray dots are data points from a randomized clinical trial and error bars are their 95% confidence intervals [65].

I_{K_r} and the L-type calcium current I_{CaL} . Blocking different combinations of currents could have opposite effects on the QT interval and is therefore a reasonable approach to test the ability of our model to predict multi-channel blockage. Fig. 11 shows the results of our model validation. Remarkably, most experimental data points fall within the 95% confidence interval of the predicted QT interval change. For dofetilide, our model accurately predicts an increasing QT interval for increasing concentrations. However, while the clinical data suggest a linear increase, our model predicts a less pronounced increase for higher dofetilide concentrations. For quinidine, the experimental data points fall almost exactly onto the black line of our mean predictions of the QT interval. For ranolazine, in excellent agreement with the clinical data, our model accurately predicts the effect of a simultaneous block of the rapid delayed rectifier potassium current I_{K_r} and the late sodium current I_{NaL} in Fig. 8 that leads to a moderate increase in the QT interval. For verapamil, both the clinical data and the model show a negligible change in the QT interval for

increasing normalized concentrations, which is the result of a larger block of the L-type calcium current I_{CaL} compared to the rapid delayed rectifier potassium current I_{Kr} . Overall, this validation confirms that our multi-fidelity Gaussian process-based surrogate model can reliably predict changes in the QT interval in response to different drugs and varying concentrations.

4. Discussion

In this work, we have presented a full sensitivity analysis and we have quantified the uncertainty induced by block-concentration measurements over the QT interval. To reduce the computational cost, we have used multi-fidelity Gaussian process regression to fuse information from a low fidelity, one-dimensional cable model with high fidelity, three-dimensional model of the heart. Cross-validation of the surrogate model revealed an error of 6% normalized by high-fidelity baseline QT interval. This level of error is small compared to the uncertainties induced by the experimental blockage measurements for different compounds in Figs. 9 and 10.

Our sensitivity analysis in Fig. 5 confirms that the rapid delayed rectifier potassium current I_{Kr} is the most influential channel to modulate the QT interval. This effect is well known and is therefore a critical component of many pro-arrhythmic drug assessment protocols [7]. However, we also quantified the relative importance of other channels. Notably, blocking the L-type calcium current I_{CaL} and the late sodium current I_{NaL} tends to shorten the QT interval, which could be useful in the co-administration of existing drugs or in the design of new drugs. For example, verapamil induces a moderate prolongation of the QT interval because the L-type calcium current I_{CaL} block compensates the effects of its rapid delayed rectifier potassium current I_{Kr} block as we can see in Figs. 9 and 10. Our findings are also in agreement with a recent pro-arrhythmic risk study that utilized I_{Kr} , I_{CaL} and I_{Na} blockages in a single cell model to predict the risk categories of 31 drugs [11]. The authors showed that, even with a different cellular model [66], blocking solely I_{Kr} increases the action potential duration, while also blocking I_{Na} or I_{CaL} decreases the action potential duration. Yet, this study did not distinguish between the late and peak components, I_{NaL} and I_{Nap} , of the sodium current, which according to our analysis in Figs. 5 and 6 have opposite effects on the QT interval. Our sensitivity analysis identified the rapid delayed rectifier potassium current I_{Kr} and the L-type calcium current I_{CaL} as the channels that have the most pronounced effects on the QT interval. This agrees well with a recent study that showed that the blocks of I_{Kr} and I_{CaL} have a better predictive power of torsades de pointes risk than the additional block of I_{Na} [67]. Sensitivity analyses are currently gaining in popularity not only in healthy but also in failing hearts, where they hold the potential to identify network regulators [68] or specific biomarkers [69] to stratify patients in cardiac disease.

Our study suggests that, from the seven channels proposed to be studied for a new regulatory framework [56], some channels have only a small effect on the QT interval. In particular, the transient outward potassium current I_{to} has a negligible elementary effects index in Fig. 5 and a nearly flat response in the main effects analysis in Fig. 6. The slow delayed rectifier potassium current I_{Ks} also has a small prolonging effect compared to the rapid delayed rectifier potassium current I_{Kr} . The elementary effect index for I_{Kr} is ten times larger than for I_{Ks} , which implies that, on average, ten times more I_{Ks} blockage is needed to achieve the same QT interval prolongation compared to blocking I_{Kr} . Although there might be other currents involved in the development of drug-induced arrhythmias [70], this suggests to remove these two currents, the transient outward potassium current I_{to} and the slow delayed rectifier potassium current I_{Ks} , from future pro-arrhythmic risk assessment studies, especially in view of reducing dimensionality and computational cost.

To quantify the uncertainty of the block-concentration measurements in the QT interval, we used a hierarchical Bayesian model [26]. For each channel, for each compound, we generated 500 samples of the Hill model parameters $\{IC_{50}, h\}$, for which we computed the QT interval and generated an overall output distribution. In accordance with our sensitivity analysis, we observed that the way the uncertainty propagates into the QT interval is highly mediated by the uncertainty in the rapid delayed rectifier potassium current I_{Kr} block measurements in Fig. 9. This finding suggests an efficient strategy for additional experiments: Improving the measurements of the rapid delayed rectifier potassium current I_{Kr} block will have the greatest impact on reducing the uncertainty of the model output. We also showed that this uncertainty tends to increase as the concentration increases. However, for most compounds, the level of uncertainty stabilizes after an initial increase. This can be explained by the nature of the Hill model, which is designed to return zero block at zero concentration. Thus, the stable uncertainty at higher concentrations might represent the truly experimental uncertainty that is propagated.

Our final validation in Fig. 11 displays an excellent agreement between our model and experimental measurements. The validation data originates from a randomized clinical trial [65] and was not previously used to calibrate our model. The drugs used for our validation block the most significant currents of our sensitivity analysis, the rapid and slow rapid and slow delayed rectifier potassium currents I_{Kr} and I_{Ks} , the L-type calcium current I_{CaL} , the late sodium current I_{NaL} , and the transient outward potassium current I_{to} . The validation data include pairs of channels with opposite effects on the QT interval, such as ranolazine with I_{Kr} and I_{NaL} and verapamil with I_{Kr} and I_{CaL} . The validation in Fig. 11 quantifies the predictive power of our model and highlights its ability to capture the simultaneous blockage of different channels. The large spread of our predictions highlights the difficulties of making predictions based on noisy experiments. By assimilating more data, we could narrow our predictions to levels comparable to the experimentally measured QT intervals.

Gaussian process regression has become increasingly popular throughout the past decade. Its applications to cardiac mechanics range from uncertainty quantification to inverse problems and optimization [71]. In a wide variety of engineering problems, Gaussian process regression has been applied to multi-fidelity problems [59,60]. However, to our knowledge, this is the first time that this technique has been applied to elementary effect indices with their associated variance. While multi-fidelity methods have recently been proposed for the uncertainty quantification of cardiac activation sequences [72], here, we use these techniques to characterize the effect of drugs on cardiac activation. Our framework provides an efficient and robust methodology to perform sensitivity analysis and uncertainty quantification for a scalar quantity of interest, in our case, the QT interval.

Our work has a few limitations. First, it is well known that the QT interval alone has a poor specificity as predictor of drug-induced arrhythmias [8]. However, it has a great sensitivity, which implies that many compounds that generate torsades de pointes do indeed prolong the QT interval. In addition to identifying channel blocks that prolong the QT interval, our method also identified channel blocks that shorten the QT interval, I_{CaL} and I_{NaL} , which could be used as inhibitors of drug-induced arrhythmias. Second, here we have based our low fidelity model on a one-dimensional transmural cable. Since the T wave is a result of both transmural and apex-to-base gradients, it would be interesting to include a second low fidelity model based on a one-dimensional apex-to-base cable [52] and explore to which extent this changes the results of our study. Third, here we focused on one specific feature of the electrocardiogram. Our methodology can be equally useful to study, for example, T wave morphology [73], and we expect it to accurately recapitulate its effect on the QT interval. Fourth, here we only considered the QT interval, as opposed to other electrocardiogram traces that could reveal additional information about the effects of specific drugs [65]. Fifth, our model does not take into account gender differences in the QT interval [74]. We could incorporate these differences by making modular changes to the ion channel dynamics of the cellular model [75]. In the future, it would be interesting to quantify gender differences via population variability [76]. Finally, we have assumed a particular electrode position, a particular cellular model [39], a specific heart rate, and a specific distribution of cell types [15], all of which could influence our predictions of the QT interval. In the future, we would also like to quantify the uncertainties of these parameters in the predictions of the model. Overall, this study is only a very first step towards systematically using sensitivity analysis and uncertainty quantification in pro-arrhythmic drug assessment. It opens a wide variety of opportunities to quantify signatures in the electrocardiogram that could be used as early predictors of drug-induced arrhythmias. For example, our method is also capable of including more levels of fidelity to improve the predictions of drug risk bio-markers. These could include changes in single cell models or experimental data from optical mapping [77,78] or dynamic patch clamp experiments [79]. Beyond electrophysiology applications, we could use this approach to integrate different sources of information in problems in cardiac mechanics [80].

In conclusion, this study quantified both the sensitivity and the uncertainty involved in drug-induced QT prolongation. Using machine learning techniques, we combined high-resolution three-dimensional modeling with low-resolution one-dimensional modeling to precisely characterize how different compounds modulate electrocardiogram recordings associated with an increased pro-arrhythmic risk. We envision that our methods and results will support the design of safe and effective drugs that avoid the risk of torsades de pointes.

Acknowledgments

This model was developed within the Dassault Systèmes Living Heart Project as part of a collaboration with Pfizer Inc. We acknowledge stimulating discussions with Anna Sher at the Internal Medicine Research Unit of Pfizer Inc., Cambridge. This study was supported by the Stanford School of Engineering Fellowship (USA), the Becas Chile-Fulbright Fellowship (Chile), the Stanford Bio-X IIP Seed Grant (USA), and the National Institutes of Health (USA) Grant U01-HL119578.

References

- [1] D.P. Zipes, H.J.J. Wellens, Sudden cardiac death, *Circulation* 98 (21) (1998) 2334–2351.
- [2] Y. Yap, A. Camm, Drug induced QT prolongation and torsades de pointes, *Heart* 89 (11) (2003) 1363–1372.
- [3] A. Gupta, A.T. Lawrence, K. Krishnan, C.J. Kavinsky, R.G. Trohman, Current concepts in the mechanisms and management of drug-induced QT prolongation and torsade de pointes, *Amer. Heart J.* 153 (6) (2007) 891–899.
- [4] F. Dessertenne, La tachycardie ventriculaire a deux foyers opposes variables, *Arch. Maladies Coeur Vaisseaux* 2 (59) (1966) 263–272.
- [5] E.J. Benjamin, S.S. Virani, C.W. Callaway, A.M. Chamberlain, A.R. Chang, S. Cheng, S.E. Chiuve, M. Cushman, F.N. Delling, R. Deo, S.D. de Ferranti, J.F. Ferguson, M. Fornage, C. Gillespie, C.R. Isasi, M.C. Jiménez, L.C. Jordan, S.E. Judd, D. Lackland, J.H. Lichtman, L. Lisabeth, S. Liu, C.T. Longenecker, P.L. Lutsey, J.S. Mackey, D.B. Matchar, K. Matsushita, M.E. Mussolino, K. Nasir, M. O'Flaherty, L.P. Palaniappan, A. Pandey, D.K. Pandey, M.J. Reeves, M.D. Ritchey, C.J. Rodriguez, G.A. Roth, W.D. Rosamond, U.K. Sampson, G.M. Satou, S.H. Shah, N.L. Spartano, D.L. Tirschwell, C.W. Tsao, J.H. Voeks, J.Z. Willey, J.T. Wilkins, J.H. Wu, H.M. Alger, S.S. Wong, P. Muntner, Heart disease and stroke statistics—2018 update: A report from the american heart association, *Circulation* 137 (12) (2018) e67–e492.
- [6] N. Stockbridge, J. Morganroth, R.R. Shah, C. Garnett, Dealing with global safety issues, *Drug Saf.* 36 (2013) 167–182.
- [7] W.S. Redfern, L. Carlsson, A.S. Davis, W.G. Lynch, I. MacKenzie, S. Palethorpe, P.K.S. Siegl, I. Strang, A.T. Sullivan, R. Wallis, A.J. Camm, T.G. Hammond, Relationships between preclinical cardiac electrophysiology, clinical QT interval prolongation and torsade de pointes for a broad range of drugs: Evidence for a provisional safety margin in drug development, *Cardiovasc. Res.* 58 (1) (2003) 32–45.
- [8] G. Gintant, P. Sager, N. Stockbridge, Evolution of strategies to improve preclinical cardiac safety testing, *Nat. Rev. Drug Discov.* 15 (7) (2016) 1–15.
- [9] P. Sager, G. Gintant, J. Turner, S. Pettit, N. Stockbridge, Rechanneling the cardiac proarrhythmia safety paradigm: A meeting report from the Cardiac Safety Research Consortium, *Amer. Heart J.* 167 (3) (2014) 292–300.
- [10] T. Colatsky, B. Fermini, G. Gintant, J. Pierson, P. Sager, Y. Sekino, D. Strauss, N. Stockbridge, The comprehensive in vitro proarrhythmia assay (CiPA) initiative – Update on progress, *J. Pharmacol. Toxicol. Methods* 81 (2016) 15–20.
- [11] G. Mirams, Y. Cui, A. Sher, M. Fink, J. Cooper, B. Heath, N. McMahon, D. Gavaghan, D. Noble, Simulation of multiple ion channel block provides improved early prediction of compounds' clinical torsadogenic risk, *Cardiovasc. Res.* 91 (1) (2011) 53–61.
- [12] D. Hurtado, S. Castro, A. Gizzi, Computational modeling of non-linear diffusion in cardiac electrophysiology: A novel porous-medium approach, *Comput. Methods Appl. Mech. Engrg.* 300 (2016) 70–83.
- [13] N. Cusimano, A. Bueno-Orovio, I. Turner, K. Burrage, On the order of the fractional Laplacian in determining the spatio-temporal evolution of a space-fractional model of cardiac electrophysiology, *PLoS One* 10 (12) (2015) 1–16.
- [14] N. Cusimano, L. Gerardo-Giorda, A space-fractional monodomain model for cardiac electrophysiology combining anisotropy and heterogeneity on realistic geometries, *J. Comput. Phys.* 362 (2018) 409–424.
- [15] F. Sahli Costabal, J. Yao, A. Sher, E. Kuhl, Predicting critical drug concentrations and torsadogenic risk using a multiscale exposure-response simulator, *Prog. Biophys. Mol. Biol.* (2018) <http://dx.doi.org/10.1016/j.pbiomolbio.2018.10.003>.
- [16] C. Obiol-Pardo, J. Gomis-Tena, F. Sanz, J. Saiz, M. Pastor, A multiscale simulation system for the prediction of drug-induced cardiotoxicity, *J. Chem. Inf. Model.* 51 (2) (2011) 483–492.
- [17] K. Beattie, C. Luscombe, G. Williams, J. Munoz-Muriedas, D. Gavaghan, Y. Cui, G. Mirams, Evaluation of an in silico cardiac safety assay: using ion channel screening data to predict QT interval changes in the rabbit ventricular wedge, *J. Pharmacol. Toxicol. Methods* 68 (1) (2013) 88–96.
- [18] F. Sahli Costabal, J. Yao, E. Kuhl, Predicting drug-induced arrhythmias by multiscale modeling, *Int. J. Numer. Methods Biomed. Eng.* 34 (2018) e2964.
- [19] F. Sahli Costabal, J. Yao, E. Kuhl, Predicting the cardiac toxicity of drugs using a novel multiscale exposure-response simulator, *Comput. Methods Biomech. Biomed. Eng.* 21 (2018) 232–246.
- [20] W. Crumb, J. Vicente, L. Johannessen, D. Strauss, An evaluation of 30 clinical drugs against the comprehensive in vitro proarrhythmia assay (CiPA) proposed ion channel panel, *J. Pharmacol. Toxicol. Methods* 81 (2016) 251–262.
- [21] S. Sankaran, A.L. Marsden, A stochastic collocation method for uncertainty quantification and propagation in cardiovascular simulations, *J. Biomech. Eng.* 133 (2011) 031001.
- [22] T. Krogh-Madsen, A.F. Jacobsen, F.A. Ortega, D.J. Christini, Global optimization of ventricular myocyte model to multi-variable objective improves predictions of drug-induced torsades de pointes, *Front. Physiol.* 8 (2017) 1059.
- [23] H. Ashikaga, J.G. James, Inter-scale information flow as a surrogate for downward causation that maintains spiral waves, *Chaos* 28 (2018) 075306.
- [24] N.S. LaVigne, N. Holt, M.J. Hoffman, E.M. Cheery, Effects of model error on cardiac electrical wave state reconstruction using data assimilation, *Chaos* 29 (2017) 093911.
- [25] H. Ashikaga, A. Asgari-Targhi, Locating order-disorder phase transition in a cardiac system, *Sci. Rep.* 8 (2018) 1967.
- [26] R.H. Johnstone, R. Bardenet, D.J. Gavaghan, G.R. Mirams, Hierarchical bayesian inference for ion channel screening dose-response data, *Wellcome Open Res.* 1 (2016).
- [27] K.C. Chang, S. Dutta, G.R. Mirams, K.A. Beattie, J. Sheng, P.N. Tran, M. Wu, W.W. Wu, T. Cotlasky, D.G. Strauss, Z. Li, Uncertainty quantification reveals the importance of data variability and experimental design considerations for in silico proarrhythmia risk assessment, *Front. Physiol.* 8 (2017) 917.
- [28] F. Sahli Costabal, J.S. Choy, K.L. Sack, J.M. Guccione, G. Kassab, E. Kuhl, Multiscale characterization of heart failure, *Acta Biomater.* (2019) <http://dx.doi.org/10.1016/j.actbio.2018.12.053>.
- [29] P. Perdikaris, D. Venturi, G.E. Karniadakis, Multifidelity information fusion algorithms for high-dimensional systems and massive data sets, *SIAM J. Sci. Comput.* 38 (4) (2016) B521–B538.

- [30] S. Göktepe, E. Kuhl, Computational modeling of cardiac electrophysiology: A novel finite element approach, *Internat. J. Numer. Methods Engrg.* 79 (2) (2009) 156–178.
- [31] A. Quarteroni, T. Lassila, S. Rossi, R. Ruiz-Baier, Integrated heart – Coupling multiscale and multiphysics models for the simulation of the cardiac function, *Comput. Methods Appl. Mech. Engrg.* 314 (2017) 345–407.
- [32] S. Göktepe, E. Kuhl, Electromechanics of the heart: A unified approach to the strongly coupled excitation-contraction problem, *Comput. Mech.* 45 (2–3) (2010) 227–243.
- [33] F. Sahli Costabal, F.A. Concha, D.E. Hurtado, E. Kuhl, The importance of mechano-electrical feedback and inertia in cardiac electromechanics, *Comput. Methods Appl. Mech. Engrg.* 320 (2017) 352–368.
- [34] H. Dal, S. Göktepe, M. Kaliske, E. Kuhl, A fully implicit finite element method for bidomain models of cardiac electromechanics, *Comput. Methods Appl. Mech. Engrg.* 253 (2013) 323–336.
- [35] S. Göktepe, J. Wong, E. Kuhl, Atrial and ventricular fibrillation: Computational simulation of spiral waves in cardiac tissue, *Arch. Appl. Mech.* 80 (5) (2010) 569–580.
- [36] J. Wong, S. Göktepe, E. Kuhl, Computational modeling of electrochemical coupling: A novel finite element approach towards ionic models for cardiac electrophysiology, *Comput. Methods Appl. Mech. Engrg.* 200 (2011) 3139–3158.
- [37] N. Zemzemi, M.O. Bernabeu, J. Saiz, J. Cooper, P. Pathmanathan, G.R. Mirams, J. Pitt-Francis, B. Rodriguez, Computational assessment of drug-induced effects on the electrocardiogram: From ion channel to body surface potentials, *British J. Pharmacol.* 168 (3) (2013) 718–733.
- [38] S. Niederer, E. Kerfoot, A. Benson, M. Bernabeu, O. Bernus, C. Bradley, E. Cherry, R. Clayton, F. Fenton, A. Garny, E. Heidenreich, S. Land, M. Maleckar, P. Pathmanathan, G. Plank, J.F. Rodriguez, I. Roy, F. Sachse, G. Seemann, O. Skavhaug, N. Smith, Verification of cardiac tissue electrophysiology simulators using an N-version benchmark, *Phil. Trans. A* 369 (2011) 4331–4351.
- [39] T. O'Hara, L. Virág, A. Varró, Y. Rudy, Simulation of the undiseased human cardiac ventricular action potential: model formulation and experimental validation, *PLoS Comput. Biol.* 7 (5) (2011) e1002061.
- [40] J. Priest, C. Gawad, K. Kahlig, J. Yu, T. O'Hara, P. Boyle, S. Rajamani, M. Clark, S. Garcia, S. Ceresnak, J. Harris, S. Boyle, F. Dewey, L. Malloy-Walton, K. Dunn, M. Grove, M. Perez, N. Neff, R. Chen, K. Maeda, A. Dubin, L. Belardinelli, J. West, C. Antolik, D. Macaya, T. Quermous, N. Trayanova, S. Quake, E. Ashley, Early somatic mosaicism is a rare cause of long-QT syndrome, *Proc. Natl. Acad. Sci.* 113 (41) (2016) 115550–11560.
- [41] K. ten Tusscher, D. Noble, P. Noble, A. Panfilov, A model for human ventricular tissue, *Amer. J. Physiol. Heart Circul. Physiol.* 286 (4) (2004) H1573–H1589.
- [42] P. Stewart, O. Aslanidi, D. Noble, P. Noble, M. Boyett, H. Zhang, Mathematical models of the electrical action potential of purkinje fibre cells, *Phil. Trans. A* 367 (1896) (2009) 2225–2255.
- [43] Dassault Systèmes, SIMULIA, Abaqus 2017, Documentation, Dassault Systèmes, Rhode Island, 2017.
- [44] M. Rausch, A. Zöllner, M. Genet, B. Baillargeon, W. Bothe, E. Kuhl, A virtual sizing tool for mitral valve annuloplasty, *Int. J. Numer. Methods Biomed. Eng.* (2017) e02788.
- [45] B. Baillargeon, N. Rebelo, D. Fox, R. Taylor, E. Kuhl, The living heart project: A robust and integrative simulator for human heart function, *European J. Mech. A Solids* 48 (2014) 38–47.
- [46] J. Okada, T. Washio, A. Maehara, S. Momomura, S. Sugiura, T. Hisada, Transmural and apicobasal gradients in repolarization contribute to T-wave genesis in human surface ECG, *Amer. J. Physiol. Heart Circul. Physiol.* 301 (1) (2011) H200–H208.
- [47] L. Perotti, S. Krishnamoorthi, N. Borgstrom, D. Ennis, W. Klug, Regional segmentation of ventricular models to achieve repolarization dispersion in cardiac electrophysiology modeling, *Int. J. Numer. Methods Biomed. Eng.* 28 (2015) e02718.
- [48] F. Sahli Costabal, D. Hurtado, E. Kuhl, Generating Purkinje networks in the human heart, *J. Biomech.* 49 (2016) 2455–2465.
- [49] M. Kotikanyadanam, S. Göktepe, E. Kuhl, Computational modeling of electrocardiograms: A finite element approach toward cardiac excitation, *Int. J. Numer. Methods Biomed. Eng.* 26 (5) (2010) 524–533.
- [50] D. Hurtado, E. Kuhl, Computational modelling of electrocardiograms: repolarisation and T-wave polarity in the human heart, *Comput. Methods Biomech. Biomed. Eng.* 17 (9) (2014) 986–996.
- [51] S. Krishnamoorthi, L.E. Perotti, N.P. Borgstrom, O. Ajijola, A. Frid, A.V. Ponnaluri, J.N. Weiss, Z. Qu, W.S. Klug, D.B. Ennis, A. Garfinkel, Simulation methods and validation criteria for modeling cardiac ventricular electrophysiology, *PLoS One* 9 (12) (2014) e114494.
- [52] A.V.S. Ponnaluri, L.E. Perotti, M. Liu, Z. Qu, J.N. Weiss, D.B. Ennis, W.S. Klug, A. Garfinkel, Electrophysiology of heart failure using a rabbit model: from the failing myocyte to ventricular fibrillation, *PLoS Comput. Biol.* 12 (2016) e1004968.
- [53] N. Kawel, E.B. Turkbey, J.J. Carr, J. Eng, A.S. Gomes, W.G. Hundley, C. Johnson, S.C. Masri, M.R. Prince, R.J. Van Der Geest, J.A. Lima, D.A. Bluemke, Middle-aged and older subjects with steady-state free precession cardiac magnetic resonance the multi-ethnic study of atherosclerosis, *Circul. Cardiovascular Imaging* 5 (4) (2012) 500–508.
- [54] D.E. Schiavazzi, A. Doostan, G. Iaccarino, A.L. Marsden, A generalized multi-resolution expansion for uncertainty propagation with application to cardiovascular modeling, *Comput. Methods Appl. Mech. Engrg.* 314 (2017) 196–221.
- [55] C.E. Rasmussen, C.K.I. Williams, *Gaussian Processes for Machine Learning*, MIT Press, Cambridge, 2006.
- [56] B. Fermini, J.C. Hancox, N. Abi-Gerges, M. Bridgland-Taylor, K.W. Chaudhary, T. Colatsky, K. Correll, W. Crumb, B. Damiano, G. Erdemli, G. Gintant, J. Imredy, J. Koerner, J. Kramer, P. Levesque, Z. Li, A. Lindqvist, C.A. Obejero-Paz, D. Rampe, K. Sawada, D.G. Strauss, J.I. Vandenberg, A new perspective in the field of cardiac safety testing through the comprehensive in vitro proarrhythmia assay paradigm, *J. Biomol. Screening* 21 (1) (2016) 1–11.
- [57] D.C. Liu, J. Nocedal, On the limited memory BFGS method for large scale optimization, *Math. Program.* 45 (1) (1989) 503–528.
- [58] E. Jones, T. Oliphant, P. Peterson, et al., *SciPy: Open source scientific tools for Python*, 2001.
- [59] M.C. Kennedy, A. O'Hagan, Predicting the output from a complex computer code when fast approximations are available, *Biometrika* 87 (1) (2000) 1–13.
- [60] P. Perdikaris, G.E. Karniadakis, Model inversion via multi-fidelity bayesian optimization: a new paradigm for parameter estimation in haemodynamics, and beyond, *J. R. Soc. Interface* 13 (118) (2016) 20151107.

- [61] M.D. Morris, Factorial sampling plans for preliminary computational experiments, *Technometrics* 33 (2) (1991) 161–174.
- [62] F. Campolongo, J. Cariboni, A. Saltelli, An effective screening design for sensitivity analysis of large models, *Environ. Model. Software* 22 (10) (2007) 1509–1518.
- [63] L. Le Gratiet, C. Cannamela, B. Iooss, A Bayesian approach for global sensitivity analysis of (multifidelity) computer codes, *SIAM/ASA J. Uncertain. Quantif.* 2 (1) (2014) 336–363.
- [64] J.E. Oakley, A. O'Hagan, Probabilistic sensitivity analysis of complex models: A Bayesian approach, *J. Roy. Statist. Soc. B* 66 (3) (2004) 751–769.
- [65] L. Johannesen, J. Vicente, J. Mason, C. Sanabria, K. Waite-Labott, M. Hong, P. Guo, J. Lin, J. Sørensen, L. Galeotti, J. Florian, M. Ugander, N. Stockbridge, D. Strauss, Differentiating drug-induced multichannel block on the electrocardiogram: randomized study of dofetilide, quinidine, ranolazine, and verapamil, *Clin. Pharmacol. Therapeutics* 96 (5) (2014) 549–558.
- [66] E. Grandi, F.S. Pasqualini, D.M. Bers, A novel computational model of the human ventricular action potential and Ca transient, *J. Mol. Cell. Cardiol.* 48 (1) (2010) 112–121.
- [67] J. Kramer, C.A. Obejero-Paz, G. Myatt, Y.A. Kuryshev, A. Bruening-Wright, J.S. Verducci, A.M. Brown, MICE Models: superior to the HERG model in predicting torsade de pointes, *Sci. Rep.* 3 (2013) 2100.
- [68] P.M. Tan, B.K. S., J.H. Omens, A.D. McCulloch, J.J. Saucerman, Predictive model identifies key network regulators of cardiomyocyte mechanosignaling, *PLoS Comput. Biol.* 13 (2017) e1005854.
- [69] C. Sanchez, G.D. Ambrosio, F. Maffessanti, E. Caiani, F. Prinzen, R. Krause, A. Auricchio, M. Potse, Sensitivity analysis of ventricular activation and electrocardiogram in tailored models of heart-failure patients, *Med. Biol. Eng. Comput.* 56 (2018) 491–504.
- [70] M. Zhong, C.M. Rees, D. Terentyev, B.-R. Choi, G. Koren, A. Karma, NCX-mediated subcellular Ca²⁺ dynamics underlying early afterdepolarizations in LQT2 cardiomyocytes, *Biophys. J.* 115 (6) (2018) 1019–1032.
- [71] P. Di Achille, A. Harouni, S. Khamzin, O. Solovyova, J.J. Rice, V. Gurev, Gaussian process regressions for inverse problems and parameter searches in models of ventricular mechanics, *Front. Physiol.* 9 (AUG) (2018) 1–17.
- [72] A. Quaglino, S. Pezzuto, P.S. Koutsourelakis, A. Auricchio, R. Krause, Fast uncertainty quantification of activation sequences in patient-specific cardiac electrophysiology meeting clinical time constraints, *Int. J. Numer. Methods Biomed. Eng.* (2018) e2985.
- [73] A. Sadrieh, L. Domanski, J. Pitt-Francis, S. Mann, E. Hodgkinson, C. Ng, M. Perry, J. Taylor, D. Gavaghan, R. Subbiah, J. Vandenberg, A. Hill, Multiscale cardiac modelling reveals the origins of notched T waves in long QT syndrome type 2, *Nature Commun.* 5 (2014) 5069.
- [74] G. Salama, G.C.L. Bett, Sex differences in the mechanisms underlying long QT syndrome, *Amer. J. Physiol. Heart Circul. Physiol.* 307 (5) (2014) H640–H648.
- [75] P.-C. Yang, C. Clancy, In silico prediction of sex-based differences in human susceptibility to cardiac ventricular tachyarrhythmias, *Front. Physiol.* 3 (2012) 360.
- [76] E. Passini, O.J. Britton, H.R. Lu, J. Rohrbacher, A.N. Hermans, D.J. Gallacher, R.J. Greig, A. Bueno-Orovio, B. Rodriguez, Human in silico drug trials demonstrate higher accuracy than animal models in predicting clinical pro-arrhythmic cardiotoxicity, *Front. Physiol.* 8 (2017) 1–15.
- [77] A. Gizzi, E. Cherry, R. Gilmour, S. Luther, S. Filippi, F. Fenton, Effects of pacing site and stimulation history on alternans dynamics and the development of complex spatiotemporal patterns in cardiac tissue, *Front. Physiol.* 4 (2013) 71.
- [78] I. Efimov, G. Salama, The future of optical mapping is bright, *Circ. Res.* 110 (10) (2012) e70–e71.
- [79] F.A. Ortega, E. Grandi, T. Krogh-Madsen, D.J. Christini, Applications of dynamic clamp to cardiac arrhythmia research: Role in drug target discovery and safety pharmacology testing, *Front. Physiol.* 8 (2018) 1099.
- [80] R. Chabiniok, V. Wang, M. Hadjicharalambous, L. Asner, J. Lee, M. Sermesant, E. Kuhl, A. Young, P. Moireau, M. Nash, D. Chapelle, D. Nordsletten, Multiphysics and multiscale modeling, data-model fusion and integration of organ physiology in the clinic: ventricular cardiac mechanics, *Interface Focus* 6 (2016) 20150083.